DOE/BC/14649--8

ANALYSIS AND EVALUATION OF INTERWELL SEISMIC LOGGING TECHNIQUES FOR RESERVOIR CHARACTERIZATION

Contract No. DE-AC22-90BC14649

Southwest Research Institute
San Antonio, Texas

Contract Date: June 29, 1990
Anticipated Completion: June 1993

Government Award: $272,600
(Current Year)

Principal Investigator: Jorge O. Parra

Project Manager: Chandra Nautiyal
Bartlesville Project Office

Reporting Period: April 1 - June 30, 1992

DISCLAIMER

SOUTHWEST RESEARCH INSTITUTE
SAN ANTONIO HOUSTON

DISCLAIMER

Portions of this document may be illegible in electronic image products. Images are produced from the best available original document.

OBJECTIVE

The objective of this three-year research program is to investigate interwell seismic logging techniques for indirectly interpreting oil and gas reservoir geology and pore fluid permeability. This work involves a balanced study of advanced theoretical and numerical modeling of seismic waves transmitted between pairs of reservoir wells combined with experimental data acquisition and processing of measurements at controlled sites as well as in full-scale reservoirs. This reservoir probing concept is aimed at demonstrating unprecedented high-resolution measurements and detailed interpretation of heterogeneous hydrocarbon-bearing formations.

SUMMARY OF TECHNICAL PROGRESS

Task 1 - Numerical Model Studies

Part of this task is to investigate the sensitivity of the *in-situ* rock-physical properties of the formation such as porosity and permeability on three-component seismograms, and the pressure, as well as phase velocity and attenuation. For this purpose we have developed software to simulate synthetic seismograms associated with a point-source (compressional wave), and a point force (shear wave), in stratified fluid-filled porous media. In addition, we have developed software to calculate phase velocity and attenuation from interwell seismic waveforms. To demonstrate the use of these capabilities we present examples to simulate seismograms and dispersion and attenuation curves.

A. Synthetic Seismograms

In this section, we present seismic responses associated with the geological formations of the Buckhorn test site in Illinois. In order to construct a representative model of formations, the rock physical properties were determined from logs. The compressional wave and shear wave velocities were determined from sonic logs recorded in boreholes A and D, (see DOE Quarterly Report, March 31, 1992). Other rock physical properties such as matrix grain density, ρ_s, and the corresponding bulk modulus, K_s, were obtained from the current literature for shale and limestone. These parameters and those determined from logs for the rock matrix, as well as the fluid properties for oil and water are given in Appendix A. Since the oil/water contact is unknown in the limestone formation, the model given in Figure 1A was assumed for the calculations. The pressure source was placed in the first borehole at a depth of 200 m, and a 12-element detector array was placed in the second borehole at 20 m away from borehole A. The detector separation used for the calculations was 2 m.

Two-component seismograms (the radial and vertical component) were calculated and the pressure for the model of Figure 1A. The seismograms illustrated in Appendix A were calculated for a source without the effect of the borehole. To properly interpret real interwell seismic data, software is currently being developed to account for the effect of the borehole. This development together with interpretation of real data will be reported in the next quarterly report.

However, to investigate the sensitivity of porosity and permeability on interwell seismic measurements, we calculated seismic responses for several model cases, in particular, when the rock-physical properties and the internal structure of the limestone formation are varied. Since the distribution of permeability and porosity are unknown, we assumed an arbitrary oil/water contact and the internal structure of the limestone layer. The seismograms illustrated in Appendix A demonstrate how the waveforms characteristics change as the rock physical properties and the internal structure of the limestone formation are varied.

B. Phase Velocity and Attenuation Models

In this second case, we calculated phase velocity and attenuation curves from synthetic data. These curves were used to determine the minimum detector separation required to generate reliable spectral ratio plots from common source gathers (when an array of detectors is used). The spectral ratio method was specialized to extract attenuation and phase velocity information from interwell seismic data. The examples given in Appendix B show phase velocity and attenuation plots for several detector separations. These plots show that the minimum detector separation to produce reliable results was about 10 m for a borehole separation of 91 m.

Task 6 - Documentation

A technical paper on the subject of interwell seismic model studies has been prepared and submitted for peer review to the *Journal of the Acoustical Society of America* in May 1992. This paper describes model results produced in this second year project. A copy of this paper is included in Appendix C.

APPENDIX A

SYNTHETIC SEISMOGRAMS

List of Symbols

THKO	=	Layer thickness
ROUO	=	Grain solid density
VPO	=	Compressional wave velocity of the matrix formation
VSO	=	Shear wave velocity of the matrix formation
SGMO	=	Bulk grain modulus of the matrix
PERMO	=	Permeability
Q	=	Quality factor
ROUFO	=	Fluid density
VFO	=	Compressional wave velocity of the fluid
VISO	=	Fluid viscosity

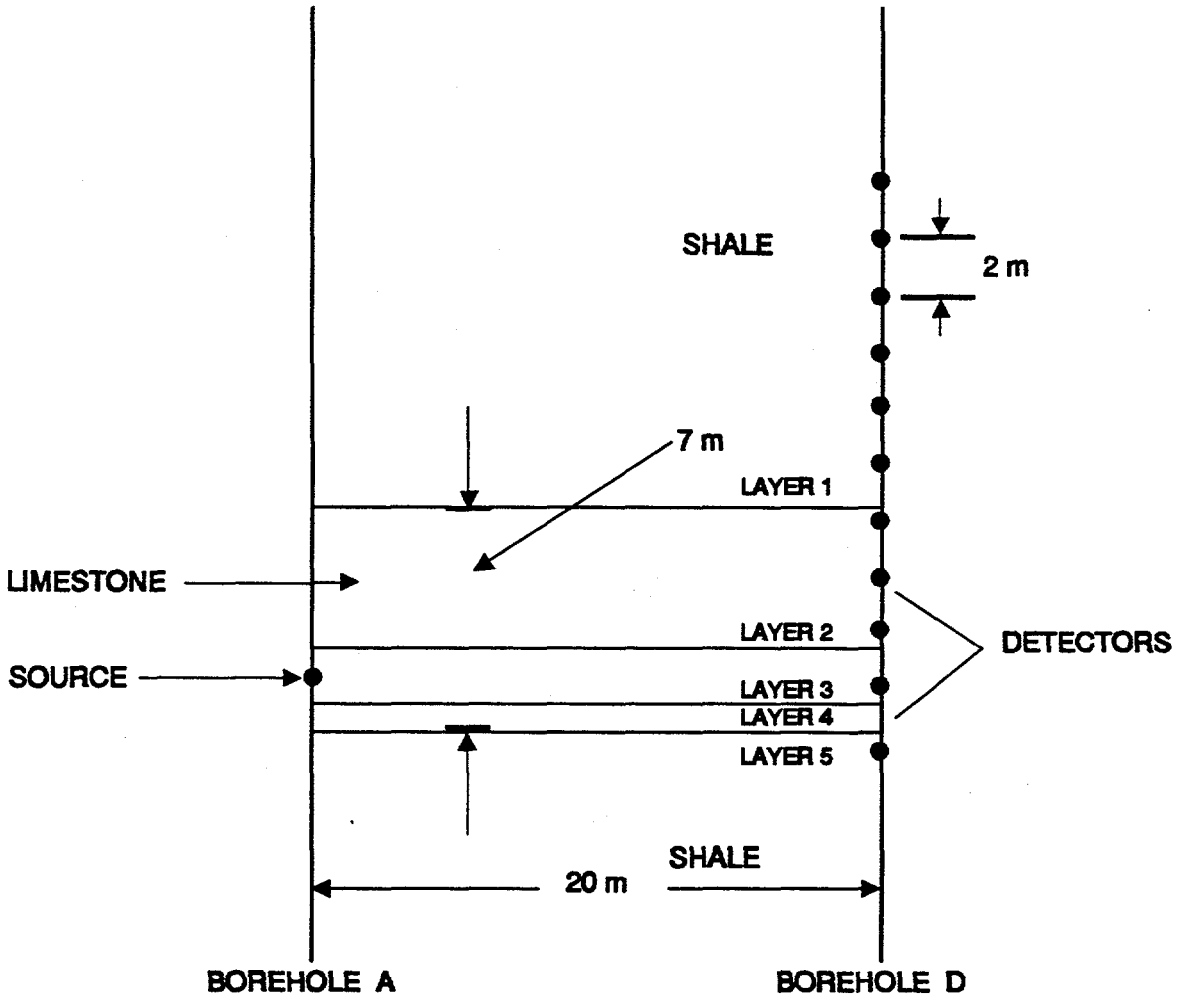

FIGURE 1A. GEOMETRY OF A FIVE LAYER EARTH MODEL

C13.in

NFD	NZ	NRT	LINK	JB	JG	NSTYPE	NROT
1	12	1	0	0	6	1	1

LL	SHORT	EPSLON	DELTA	FITFAC
0D-07	0.100D-02	0.200D-03	0.100D-01	0.100D-03

INT	DECAY	SMOOTH	RANGE	TINY
0D-00	0.400D+02	0.100D+02	0.100D+02	0.100D-10

0	ROU0 (g/cc)	VP0 (km/s)	VS0 (km/s)	SGM0/10**9 (N/m/m)	PERM0 (Darcy)	Q	PHI	ROUF0 (g/cc)	VF0 (km/s)	VIS0 (cm*g/s)
00	2.670	1.8119	1.200	26.76	0.001	0	.300	1.000	1.549	.01000
30	2.710	5.0100	3.100	74.82	0.100	0	.100	0.880	1.449	1.8000
10	2.710	3.5000	0.600	74.82	1.000	0	.150	1.000	1.549	.01000
30	2.710	5.0100	3.100	74.82	0.100	0	.100	1.000	1.549	.01000
00	2.670	1.8119	1.200	26.76	0.001	0	.300	1.000	1.549	.01000

IN	FRQMAX	DFRQ	----------	(Hz)
00	1000.00	10.00		

E-X	FORCE-Y	FORCE-Z	VOLUME
00	0.0000	0.0000	1.000

CE-R	SOURCE-T	SOURCE-Z	----------	(km)
00	0.0000	1.0035		

IVER DEPTH			----------	(km)		
70	0.9890	0.9910	0.9930	0.9950	0.9970	0.9990
10	1.0035	1.0050	1.0070	1.0090		

IVER RADIUS	----------	(km)
00		

IVER AZIMUTH	----------	(degree)
00		

LACEMENT & PRESSURE COMPONENTS (Radial, Tangential, Vertical and Pressure)

0	1	1

ED ANGLES	----------	(degree)

90.0	135.0	(X-axis w. original axes)
0.0	90.0	(Y-axis w. original axes)
90.0	45.0	(Z-axis w. original axes)

9:47 am July 2, 1992

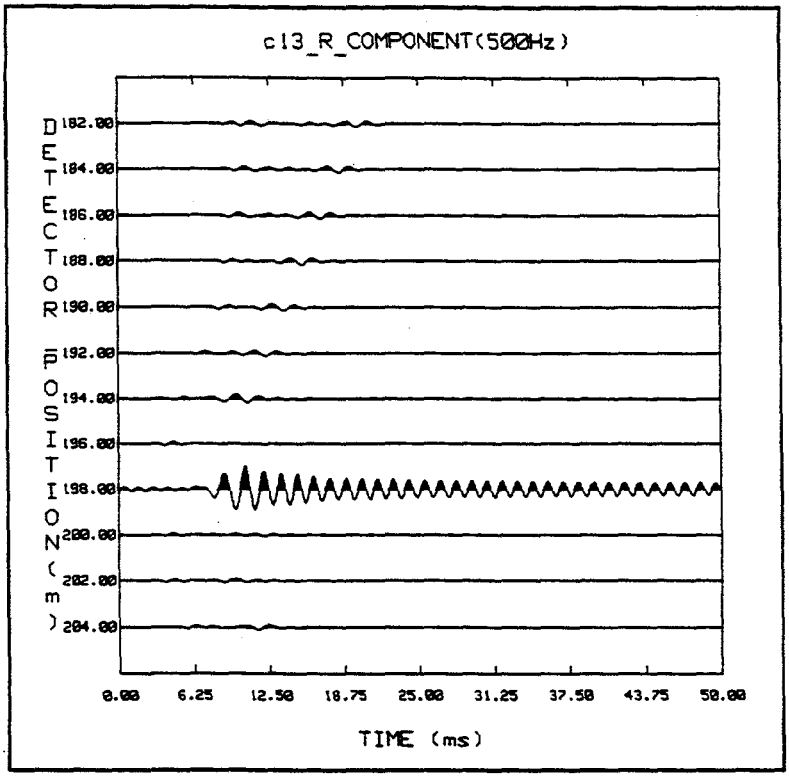

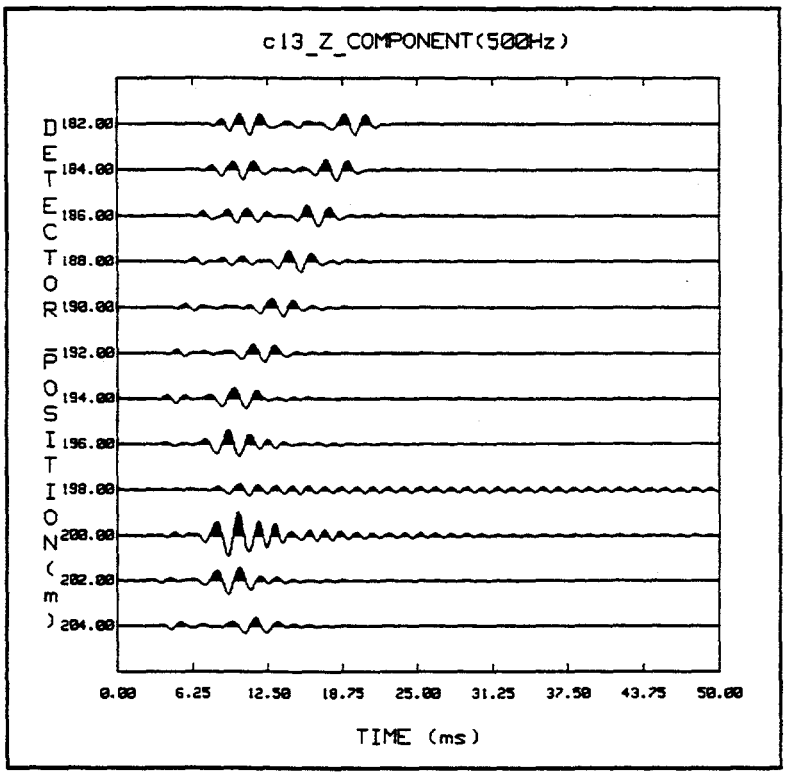

9:53 am July 2, 1992

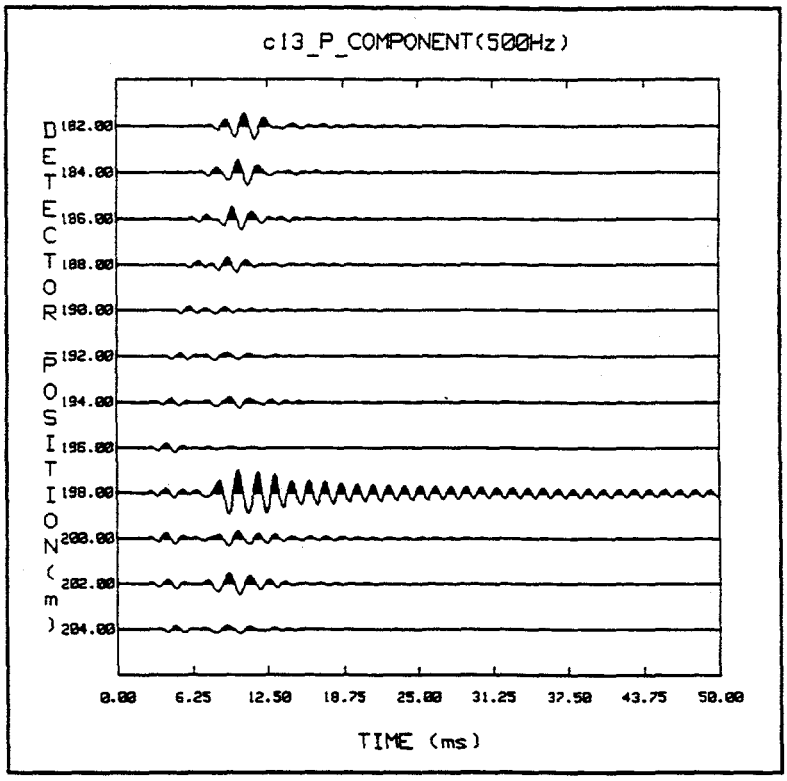

c12.in

NFD	NZ	NRT	LINK	JB	JG	NSTYPE	NROT
1	12	1	0	0	6	1	1

LL	SHORT	EPSLON	DELTA	FITFAC
0D-07	0.100D-02	0.200D-03	0.100D-01	0.100D-03

INT	DECAY	SMOOTH	RANGE	TINY
0D-00	0.400D+02	0.100D+02	0.100D+02	0.100D-10

0)	ROU0 (g/cc)	VP0 (km/s)	VS0 (km/s)	SGM0/10**9 (N/m/m)	PERM0 (Darcy)	Q	PHI	ROUF0 (g/cc)	VF0 (km/s)	VIS0 (cm*g/s)
00	2.670	1.8119	1.200	26.76	0.001	0	.300	1.000	1.549	.01000
40	2.710	5.0127	3.100	74.82	0.100	0	.100	0.880	1.449	1.8000
20	2.710	5.0000	2.700	74.82	1.000	0	.150	1.000	1.549	.01000
10	2.710	5.6394	2.700	74.82	0.100	0	.100	1.000	1.549	.01000
00	2.670	1.8119	1.200	26.76	0.001	0	.300	1.000	1.549	.01000

IN	FRQMAX	DFRQ	----------	(Hz)		
00	1000.00	10.00				
E-X	FORCE-Y	FORCE-Z	VOLUME			
00	0.0000	0.0000	1.000			
CE-R	SOURCE-T	SOURCE-Z	----------	(km)		
00	0.0000	1.0050				
IVER	DEPTH		----------	(km)		
70	0.9890	0.9910	0.9930	0.9950	0.9970	0.9990
10	1.0030	1.0050	1.0070	1.0090		
IVER	RADIUS		----------	(km)		
00						
IVER	AZIMUTH		----------	(degree)		
00						

LACEMENT & PRESSURE COMPONENTS (Radial, Tangential, Vertical and Pressure)

0	1	1		
TED	ANGLES		----------	(degree)
0	90.0	135.0	(X-axis w. original axes)	
0	0.0	90.0	(Y-axis w. original axes)	
0	90.0	45.0	(Z-axis w. original axes)	

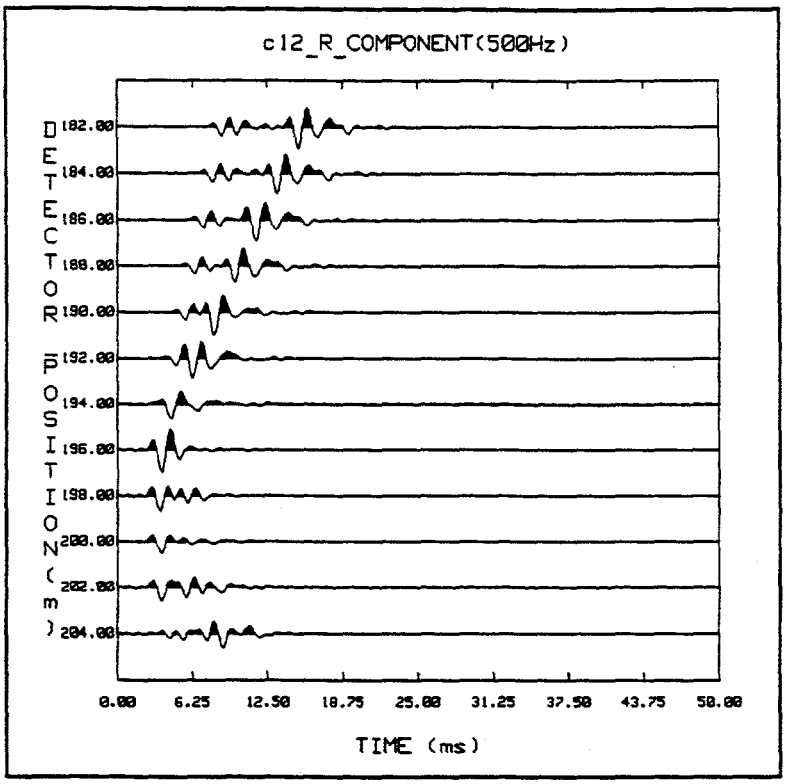
c12_R_COMPONENT(500Hz)
DETECTOR POSITION (m)
182.00
184.00
186.00
188.00
190.00
192.00
194.00
196.00
198.00
200.00
202.00
204.00
0.00
6.25
12.50
18.75
25.00
31.25
37.50
43.75
50.00
TIME (ms)

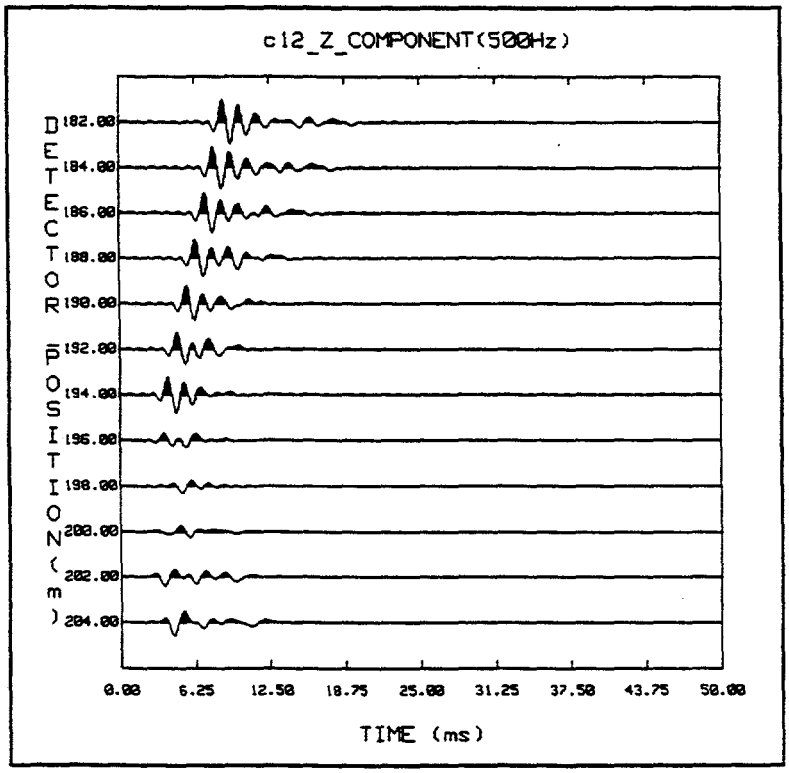
c12_Z_COMPONENT(500Hz)
DETECTOR POSITION (m)
182.00
184.00
186.00
188.00
190.00
192.00
194.00
196.00
198.00
200.00
202.00
204.00
0.00
6.25
12.50
18.75
25.00
31.25
37.50
43.75
50.00
TIME (ms)

10:32 am June 30, 1992

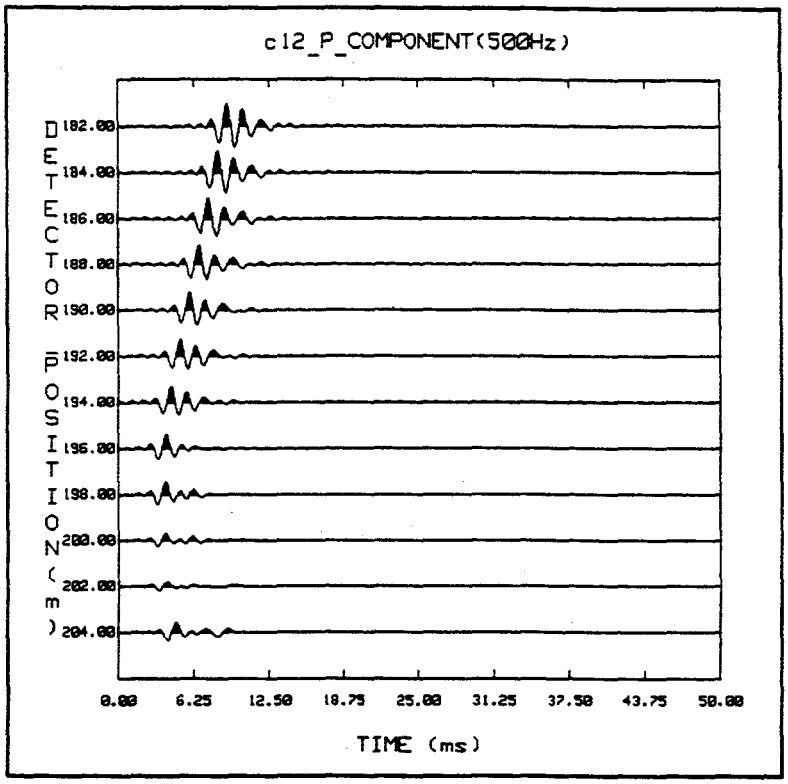

NFD	NZ	NRT	LINK	JB	JG	NSTYPE	NROT
1	12	1	0	0	6	1	1

LL	SHORT	EPSLON	DELTA	FITFAC
0D-07	0.100D-02	0.200D-03	0.100D-01	0.100D-03

INT	DECAY	SMOOTH	RANGE	TINY
0D-00	0.400D+02	0.100D+02	0.100D+02	0.100D-10

0	ROU0	VP0	VS0	SGM0/10**9	PERM0	Q	PHI	ROUF0	VF0	VIS0
)	(g/cc)	(km/s)	(km/s)	(N/m/m)	(Darcy)			(g/cc)	(km/s)	(cm*g/s)
00	2.670	1.8119	1.200	26.76	0.001	0	.300	1.000	1.549	.01000
40	2.710	5.0127	3.100	74.82	0.100	0	.100	0.880	1.449	1.8000
20	2.710	2.3160	1.000	74.82	1.000	0	.150	1.000	1.549	.01000
10	2.710	5.6394	2.700	74.82	0.100	0	.100	1.000	1.549	.01000
00	2.670	1.8119	1.200	26.76	0.001	0	.300	1.000	1.549	.01000

IN	FRQMAX	DFRQ	----------	(Hz)
00	1000.00	10.00		

E-X	FORCE-Y	FORCE-Z	VOLUME
00	0.0000	0.0000	1.000

CE-R	SOURCE-T	SOURCE-Z	----------	(km)
00	0.0000	1.0050		

IVER DEPTH			----------	(km)		
70	0.9890	0.9910	0.9930	0.9950	0.9970	0.9990
10	1.0030	1.0050	1.0070	1.0090		

IVER RADIUS	----------	(km)
00		

IVER AZIMUTH	----------	(degree)
00		

LACEMENT & PRESSURE COMPONENTS (Radial, Tangential, Vertical and Pressure)

0	1	1

TED ANGLES	----------	(degree)	
) 90.0	135.0		(X-axis w. original axes)
) 0.0	90.0		(Y-axis w. original axes)
) 90.0	45.0		(Z-axis w. original axes)

2:13 pm June 20, 1992

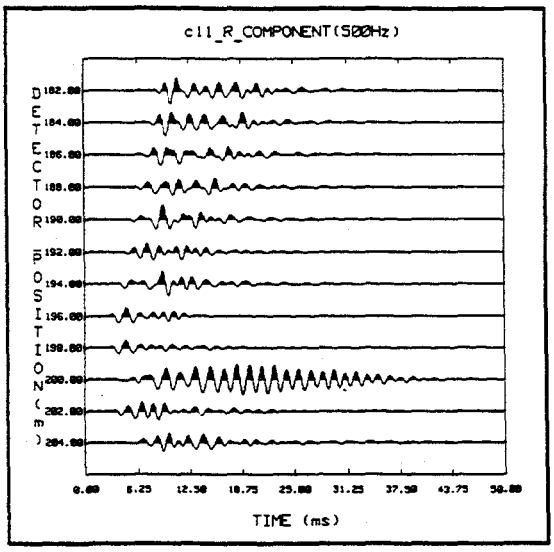

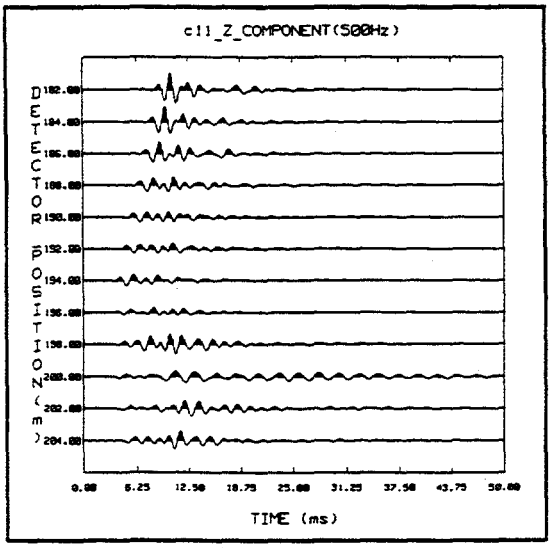

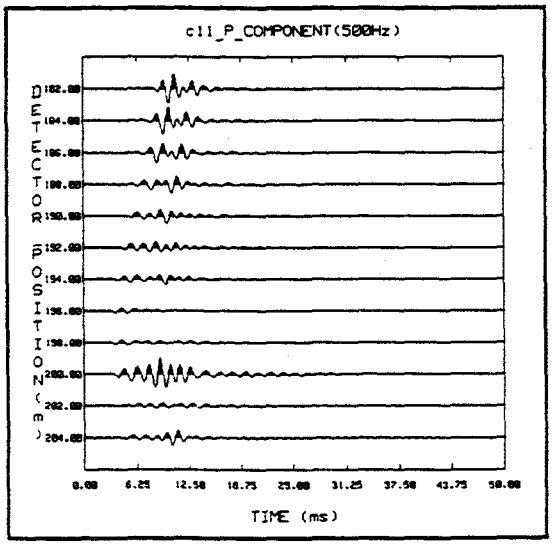

c/o. in

NFD	NZ	NRT	LINK	JB	JG	NSTYPE	NROT
1	12	1	0	0	6	1	1

LL	SHORT	EPSLON	DELTA	FITFAC
0D-07	0.100D-02	0.200D-04	0.100D-01	0.100D-03

INT	DECAY	SMOOTH	RANGE	TINY
0D-00	0.400D+02	0.100D+02	0.100D+02	0.100D-10

0	ROU0	VP0	VS0	SGM0/10**9	PERM0	Q	PHI	ROUF0	VF0	VISO
)	(g/cc)	(km/s)	(km/s)	(N/m/m)	(Darcy)			(g/cc)	(km/s)	(cm*g/s)
00	2.670	1.8119	1.200	26.76	0.001	0	.300	1.000	1.549	.01000
40	2.710	5.0127	3.100	74.82	1.000	0	.150	0.880	1.449	1.8000
20	2.710	2.3160	0.700	74.82	1.000	0	.150	1.000	1.549	.01000
10	2.710	5.6394	2.700	74.82	1.000	0	.150	1.000	1.549	.01000
00	2.670	1.8119	1.200	26.76	0.001	0	.300	1.000	1.549	.01000

IN	FRQMAX	DFRQ	----------	(Hz)		
00	1000.00	10.00				
E-X	FORCE-Y	FORCE-Z	VOLUME			
00	0.0000	0.0000	1.000			
CE-R	SOURCE-T	SOURCE-Z	----------	(km)		
00	0.0000	1.0050				
IVER	DEPTH		----------	(km)		
70	0.9890	0.9910	0.9930	0.9950	0.9970	0.9990
10	1.0030	1.0050	1.0070	1.0090		
IVER	RADIUS		----------	(km)		
00						
IVER	AZIMUTH		----------	(degree)		
00						

LACEMENT & PRESSURE COMPONENTS (Radial, Tangential, Vertical and Pressure)

0	1	1		
TED	ANGLES		----------	(degree)
)	90.0	135.0	(X-axis w. original axes)	
)	0.0	90.0	(Y-axis w. original axes)	
)	90.0	45.0	(Z-axis w. original axes)	

9:11 am June 19, 1992

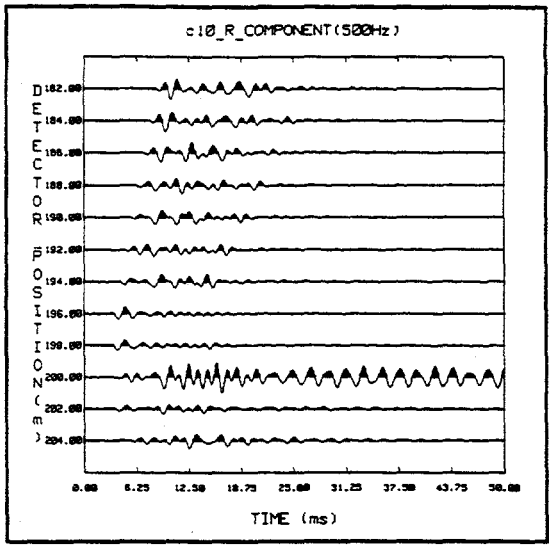

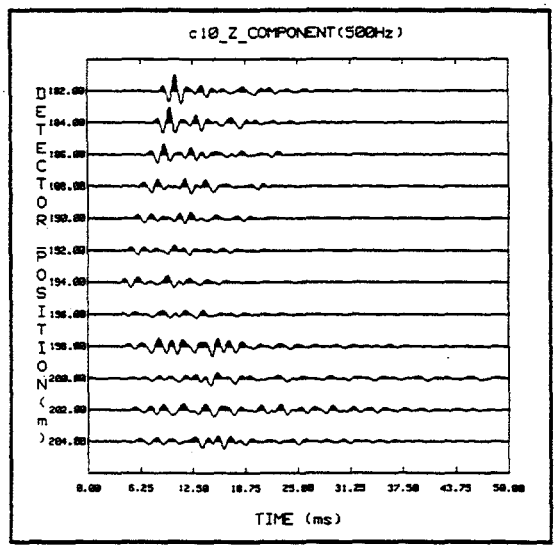

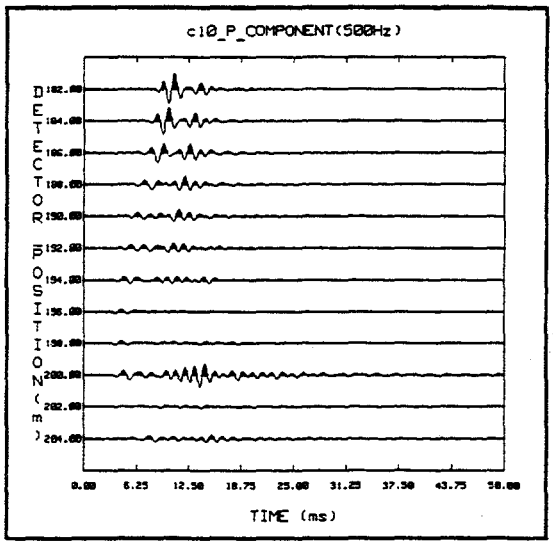

APPENDIX B

PHASE VELOCITY AND ATTENUATION PLOTS

Phase Velocity and Attenuation Plots

In this Appendix B, results from five computer runs are presented. The synthetic waveforms to generate phase velocity and attenuation curves were produced for a source in an unbounded medium having a compression wave velocity of V_p = 5000 m/s and quality factor Q = 20. The boreholes for the simulations were separated by 91.27 m, corresponding to the separation between boreholes A and E of the Buckhorn test site in Illinois. In all the computer runs a reference trace was used, which was recorded at the zero-vertical offset. The sampling time was 97.7 μsec and the reference trace started at 135 Δt and contained 100 samples. A Blackman window was used to avoid finite sampling error.

The four plots are: (1) computed phase velocity; (2) spectral ratio; (3) Q(f); and (4) $Q^{-1}(f)$.

The parameters for the five runs are shown below, as are the values for Q that was calculated (over the range of 1000-2500 Hz):

Run 1

Depth:	40 m
Start Time:	150Δt
Calc. Q:	20.58

Run 2

Depth:	40 m
Start Time:	145Δt
Calc. Q:	20.42

Run 3

Depth:	20 m
Start Time:	135Δt
Calc. Q:	18.63

Run 4

Depth:	20 m
Start Time:	140Δt
Calc. Q:	20.84

Run 5

Depth:	1 m
Start Time:	135Δt
Calc. Q:	16.79

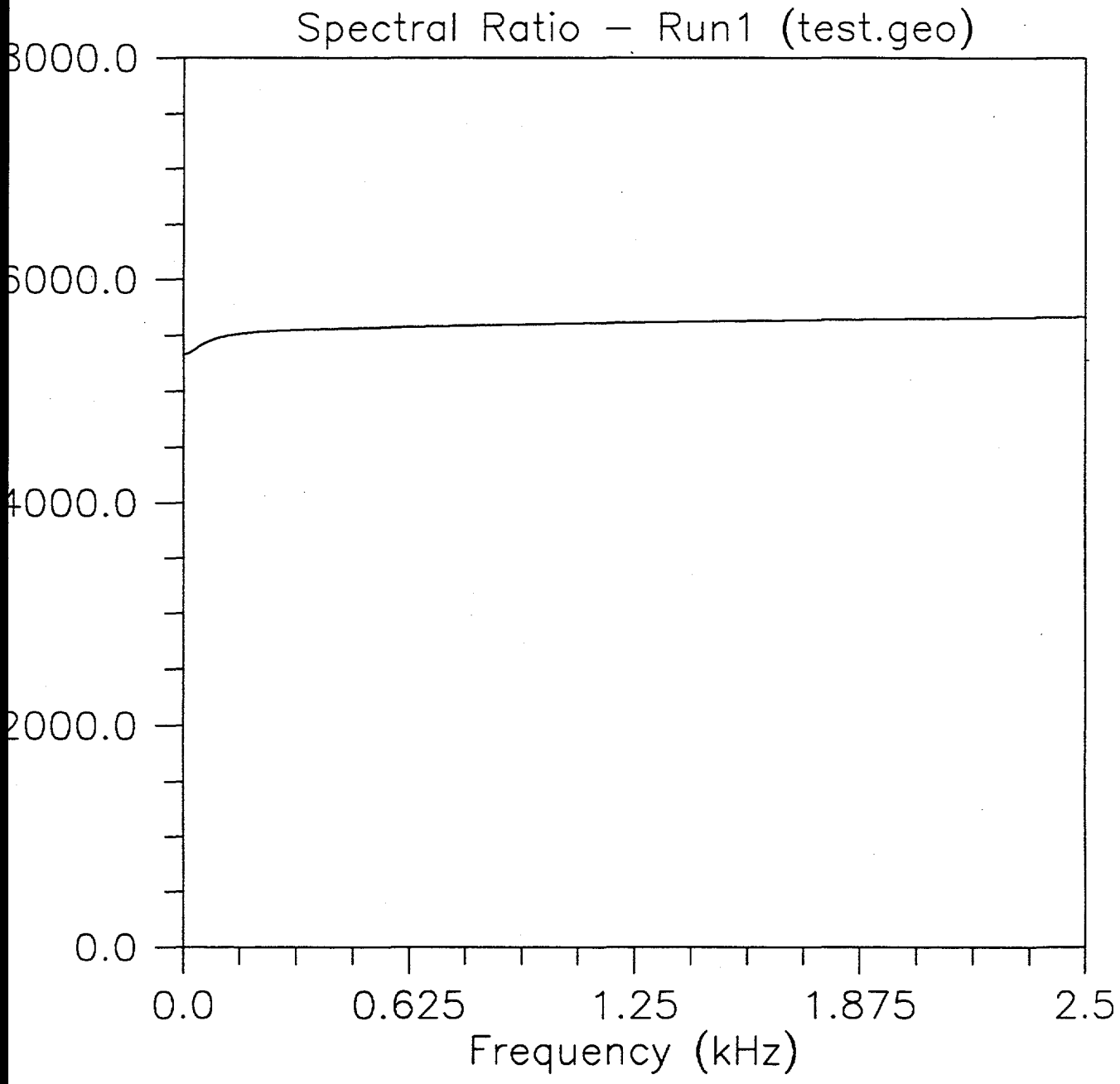
Spectral Ratio – Run1 (test.geo)
8000.0
6000.0
4000.0
2000.0
0.0
0.0
0.625
1.25
1.875
2.5
Frequency (kHz)

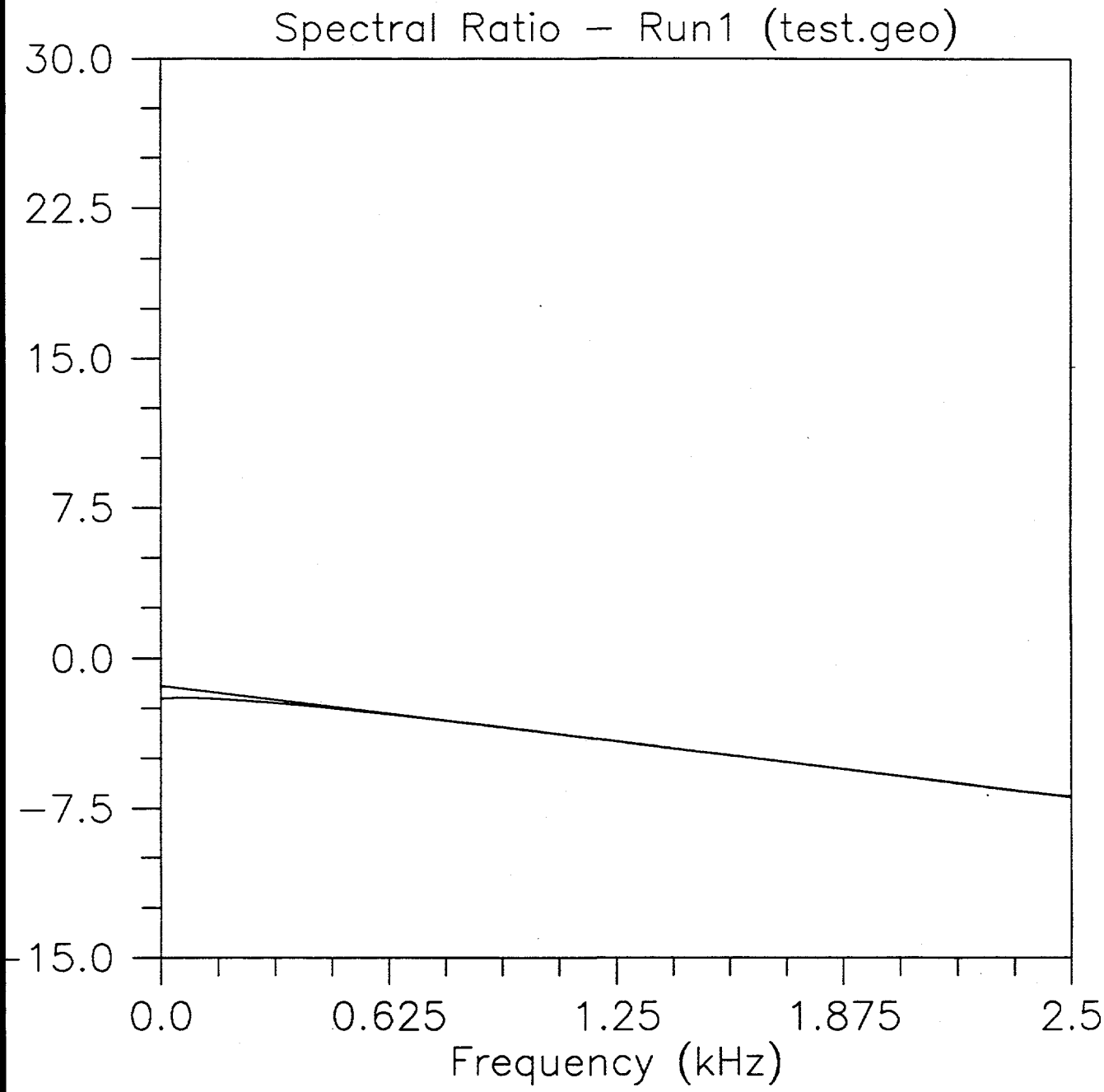
Spectral Ratio – Run1 (test.geo)
30.0
22.5
15.0
7.5
0.0
−7.5
−15.0
0.0
0.625
1.25
1.875
2.5
Frequency (kHz)

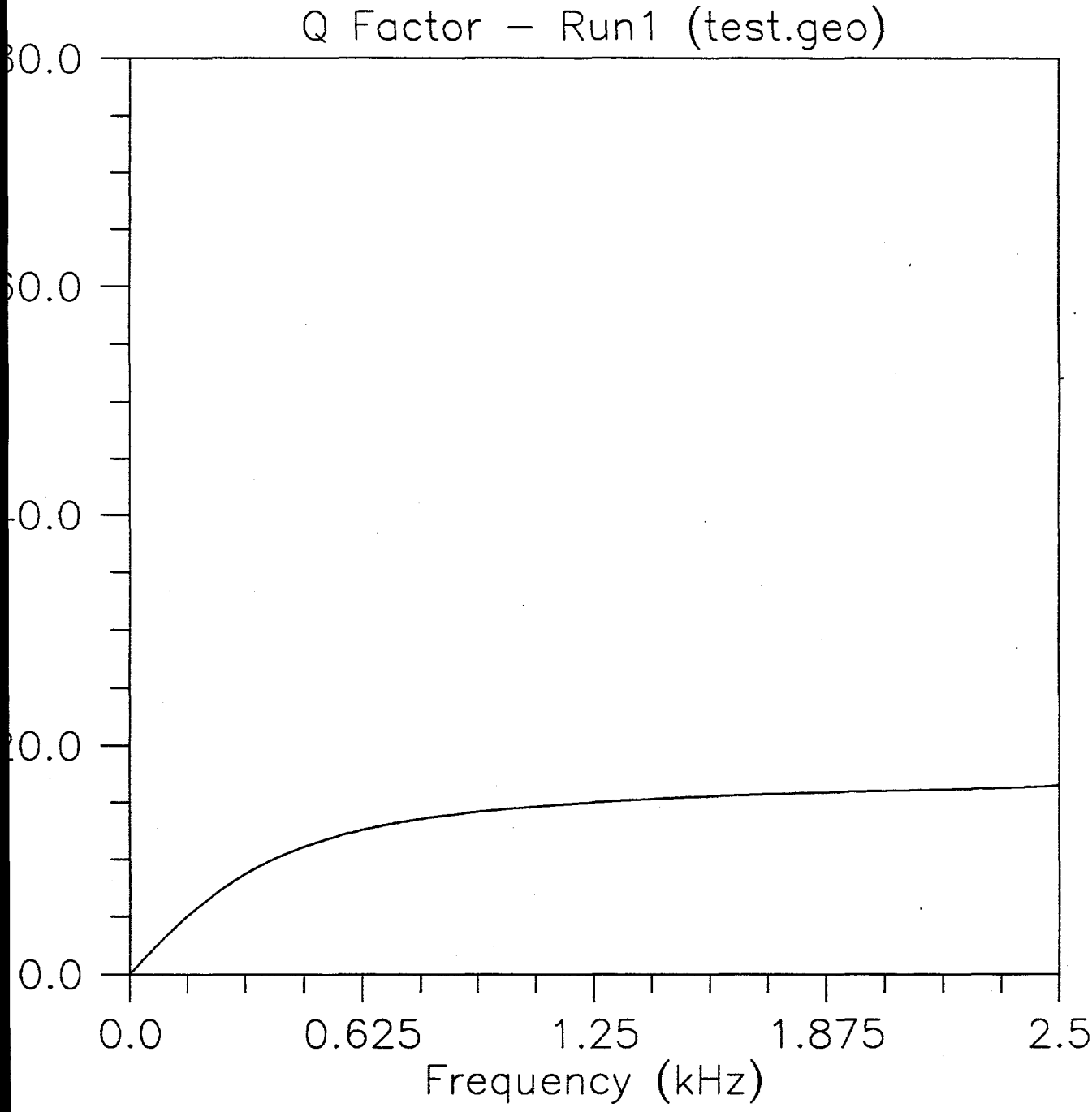
Q Factor – Run1 (test.geo)
80.0
60.0
40.0
20.0
0.0
0.0
0.625
1.25
1.875
2.5
Frequency (kHz)

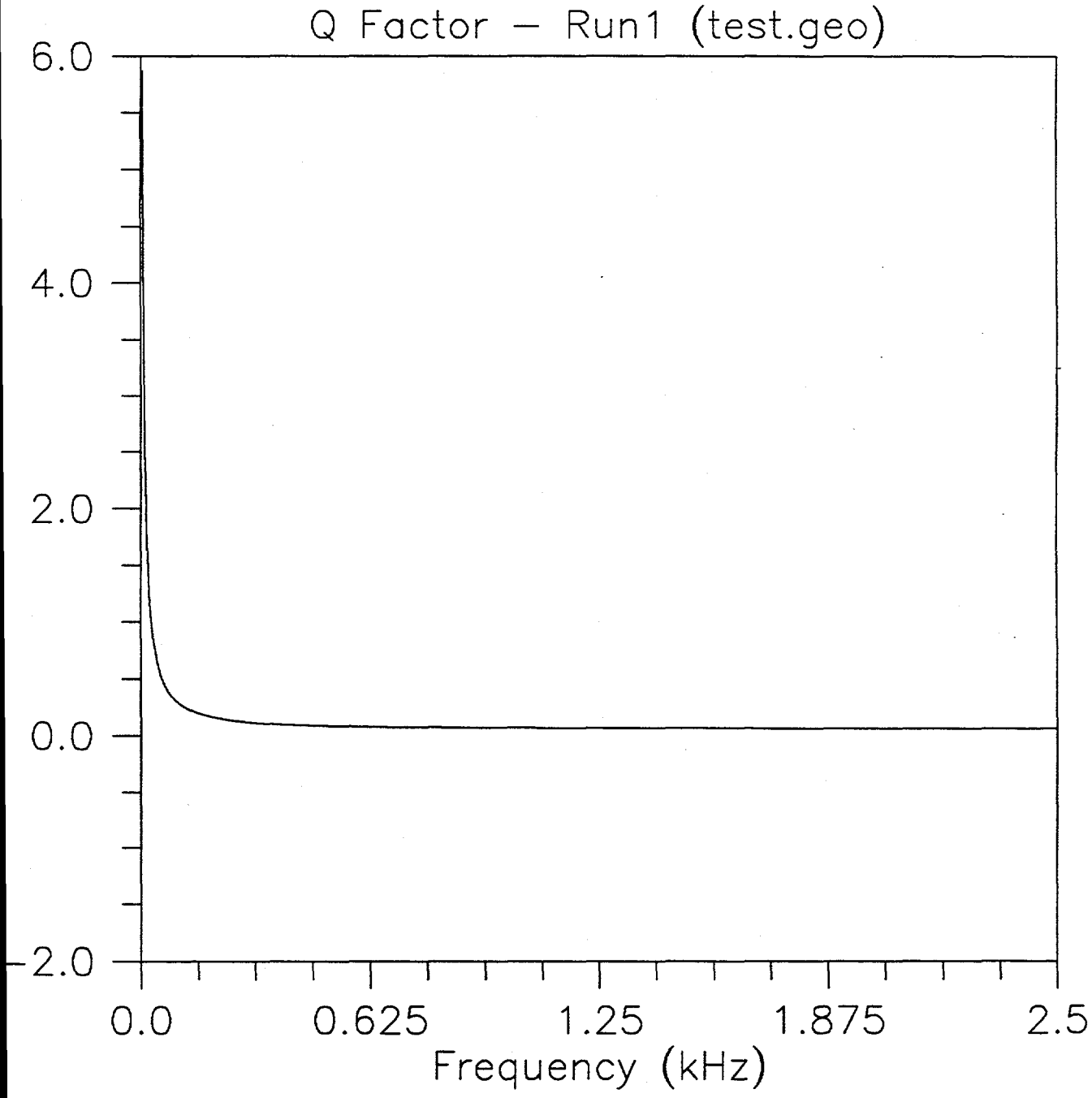
Q Factor – Run1 (test.geo)
6.0
4.0
2.0
0.0
-2.0
0.0
0.625
1.25
1.875
2.5
Frequency (kHz)

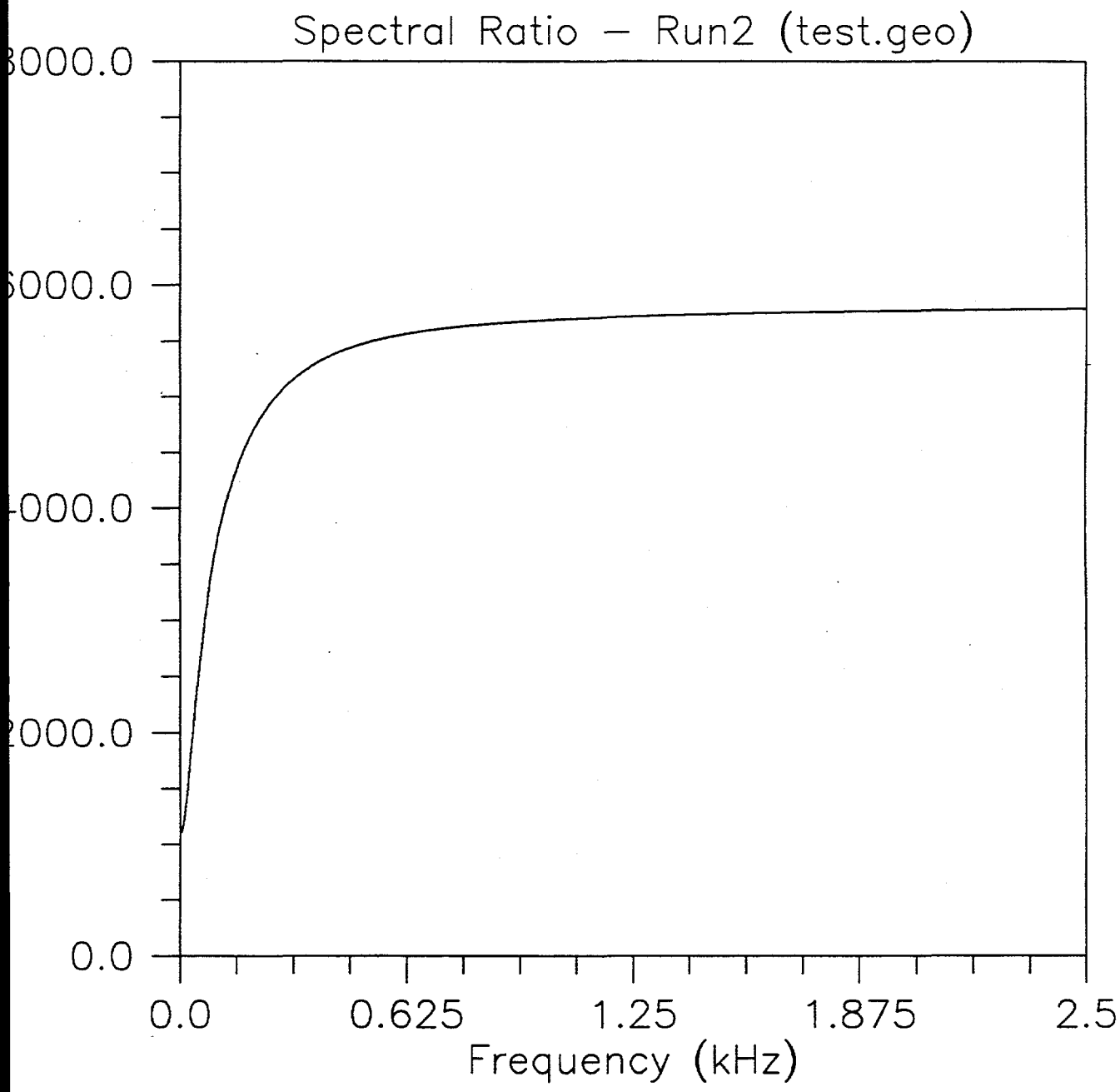
Spectral Ratio – Run2 (test.geo)
3000.0
6000.0
4000.0
2000.0
0.0
0.0
0.625
1.25
1.875
2.5
Frequency (kHz)

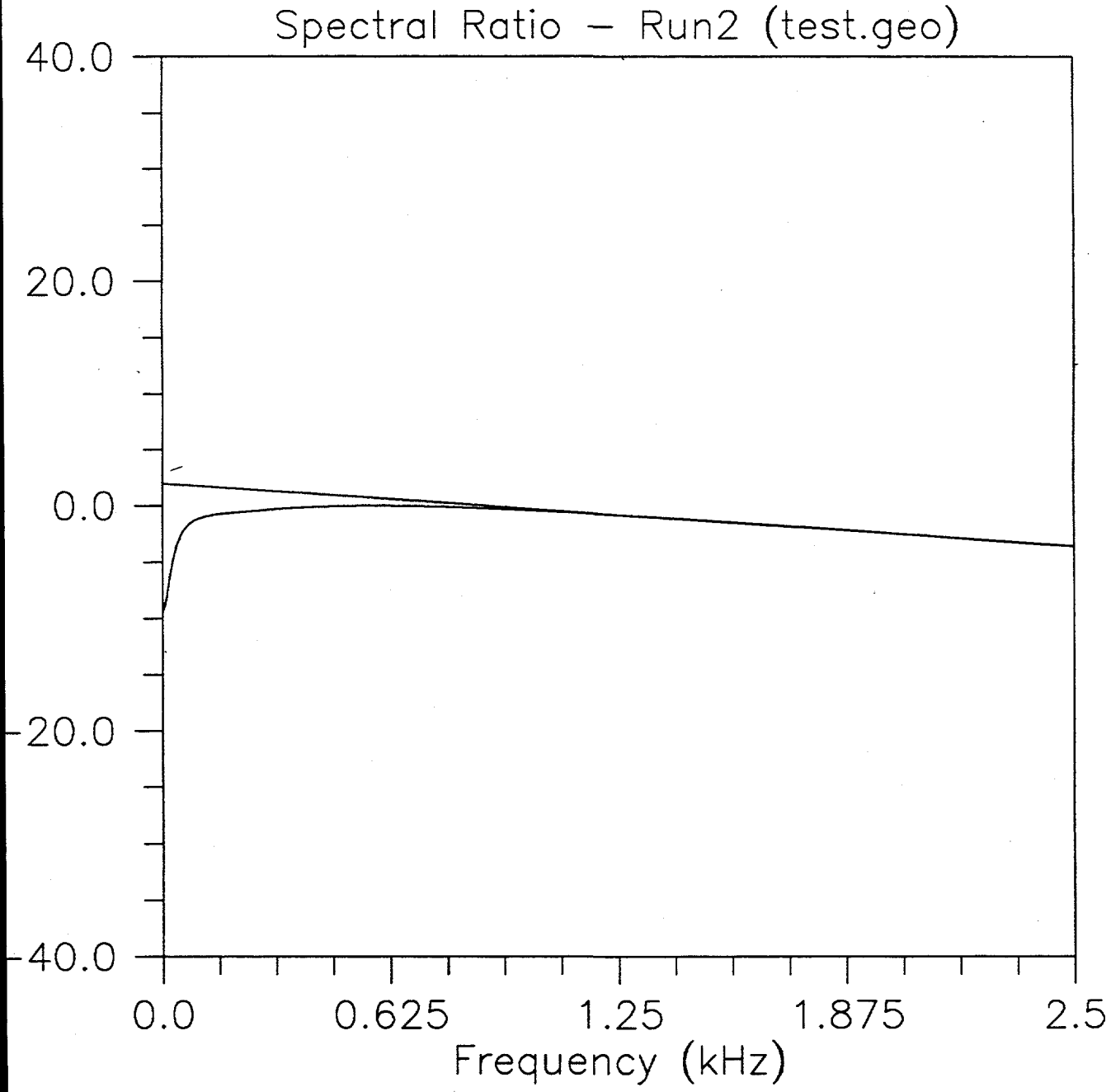
Spectral Ratio – Run2 (test.geo)
40.0
20.0
0.0
-20.0
-40.0
0.0
0.625
1.25
1.875
2.5
Frequency (kHz)

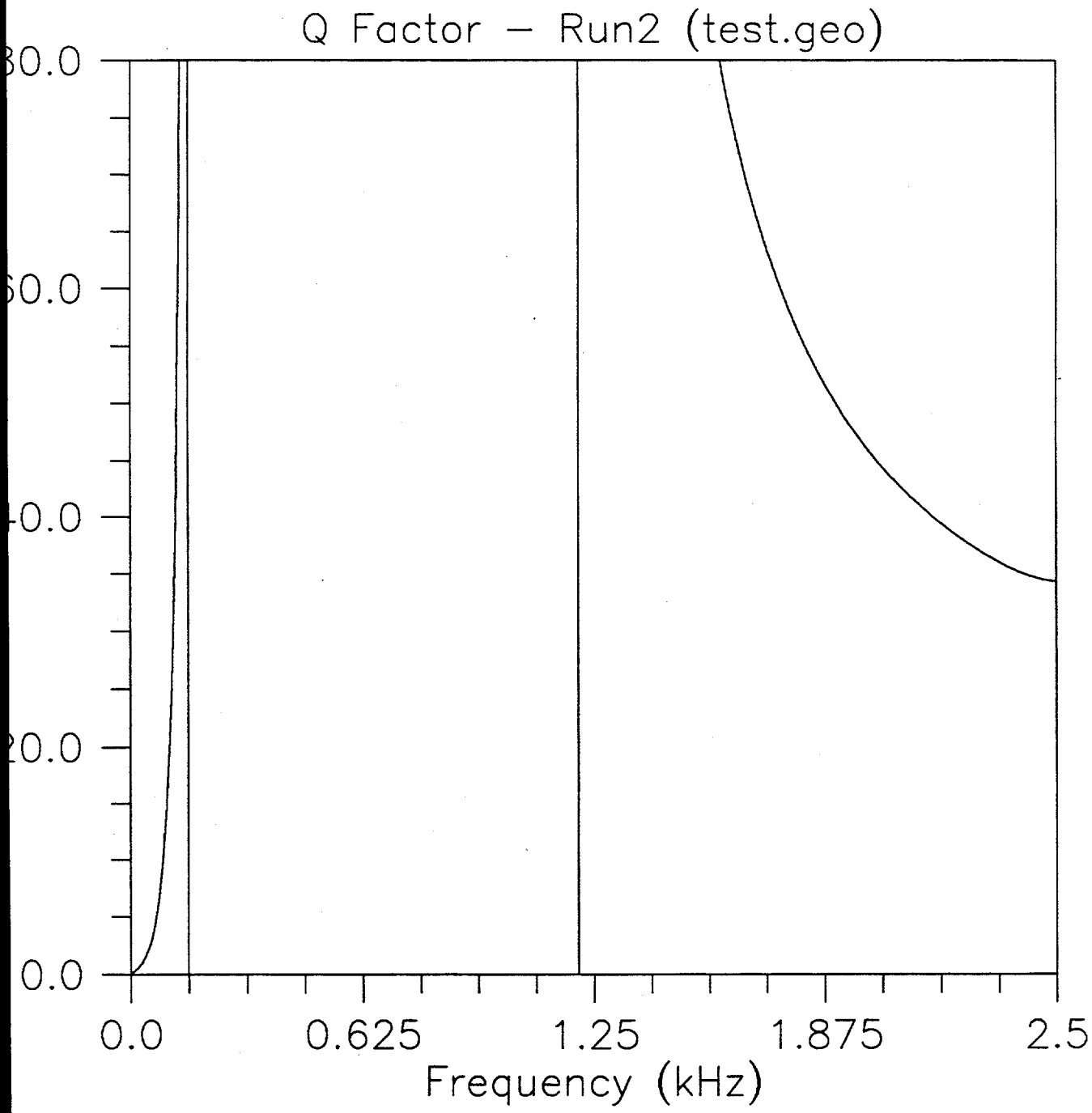
Q Factor – Run2 (test.geo)
80.0
60.0
40.0
20.0
0.0
0.0
0.625
1.25
1.875
2.5
Frequency (kHz)

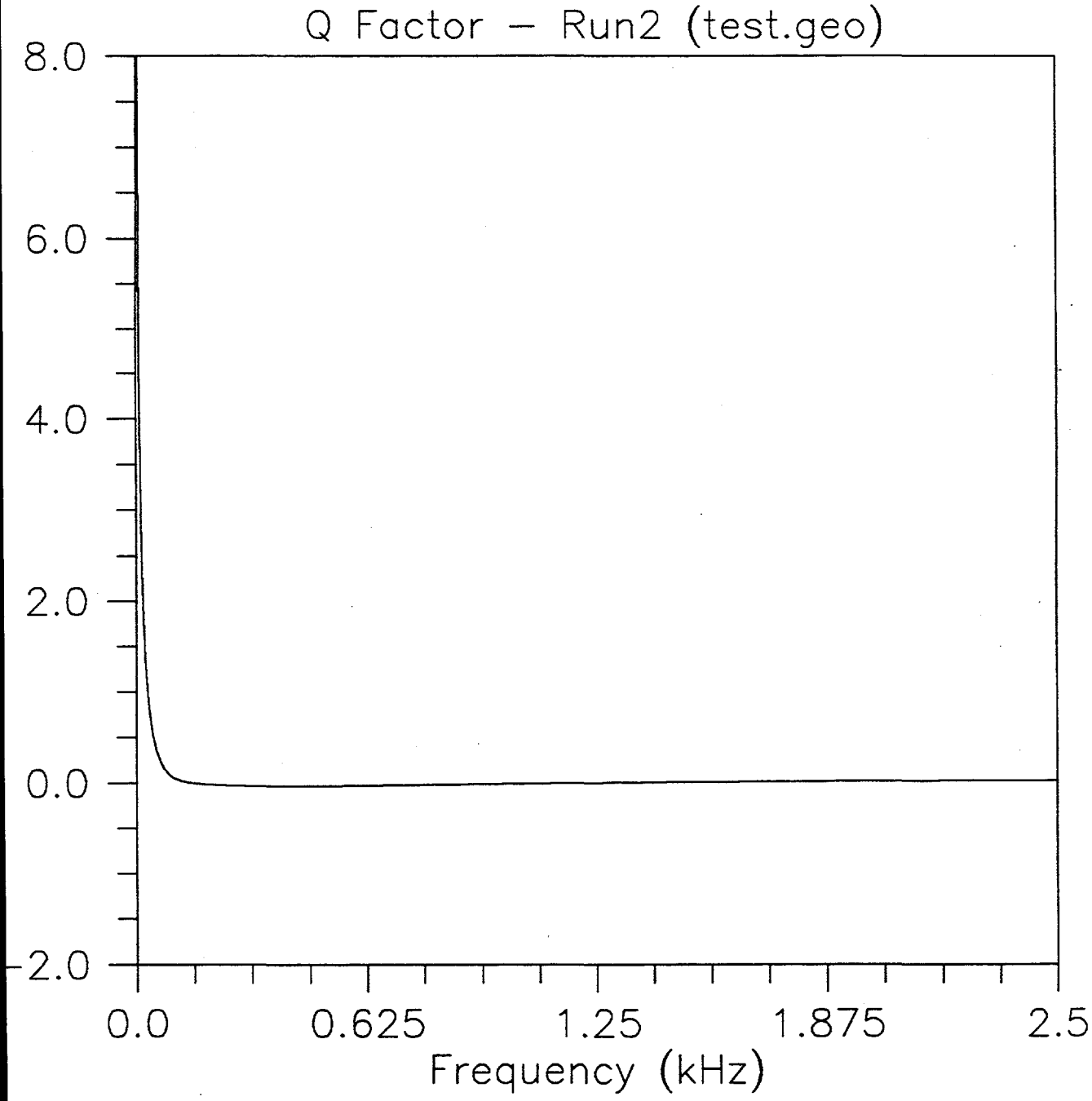
Q Factor – Run2 (test.geo)
8.0
6.0
4.0
2.0
0.0
-2.0
0.0
0.625
1.25
1.875
2.5
Frequency (kHz)

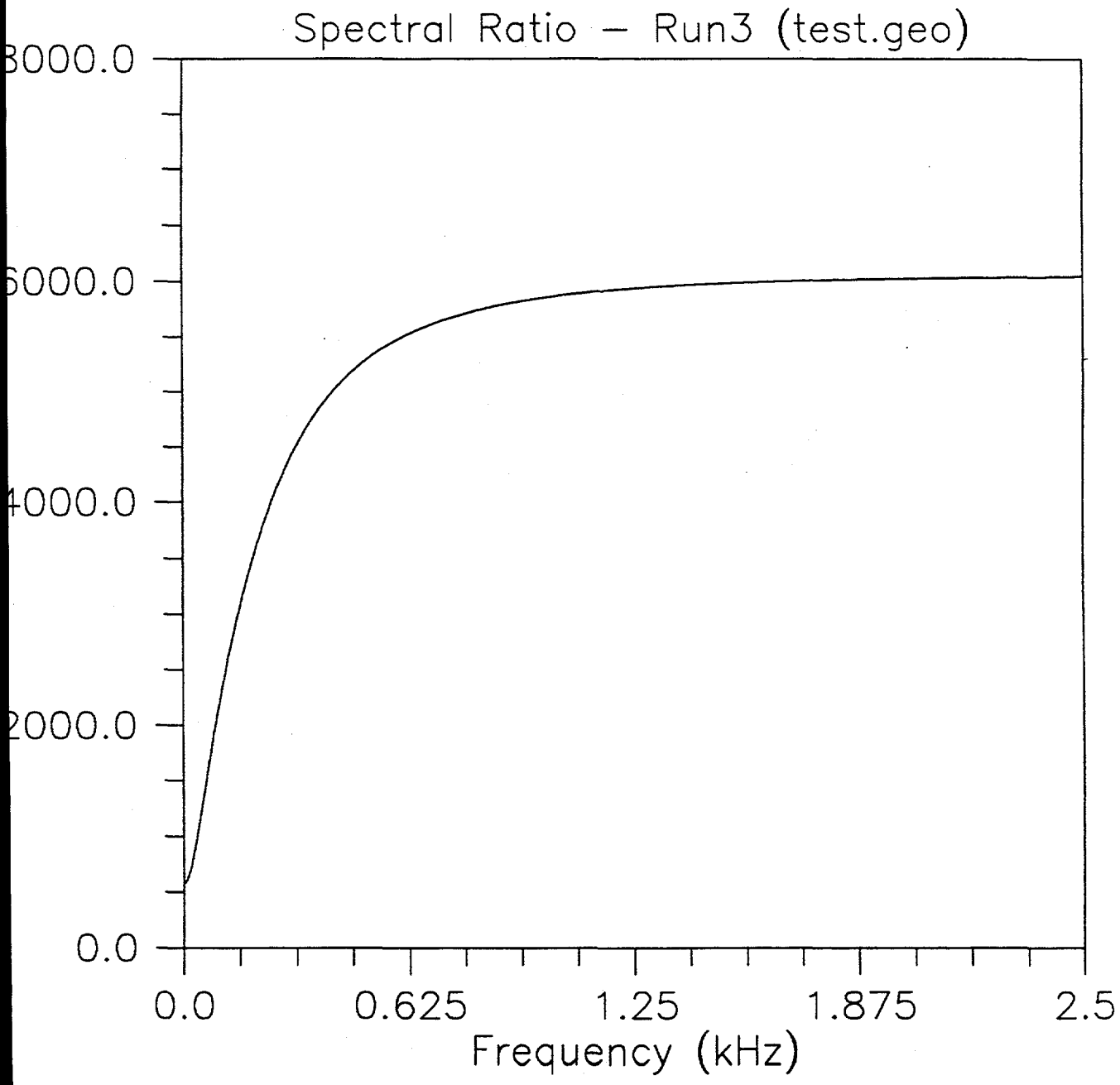
Spectral Ratio – Run3 (test.geo)
8000.0
6000.0
4000.0
2000.0
0.0
0.0
0.625
1.25
1.875
2.5
Frequency (kHz)

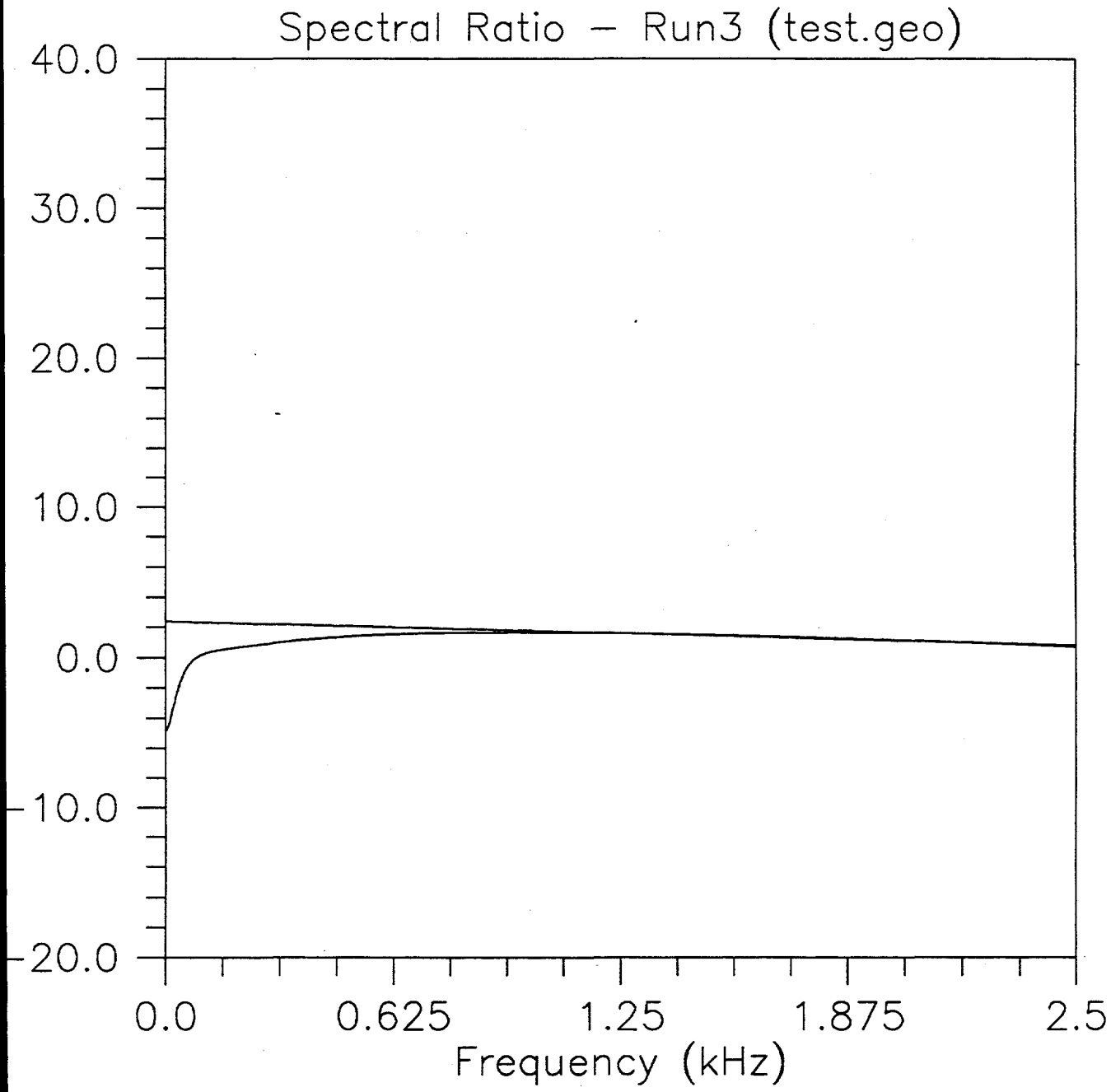
Spectral Ratio – Run3 (test.geo)
40.0
30.0
20.0
10.0
0.0
-10.0
-20.0
0.0
0.625
1.25
1.875
2.5
Frequency (kHz)

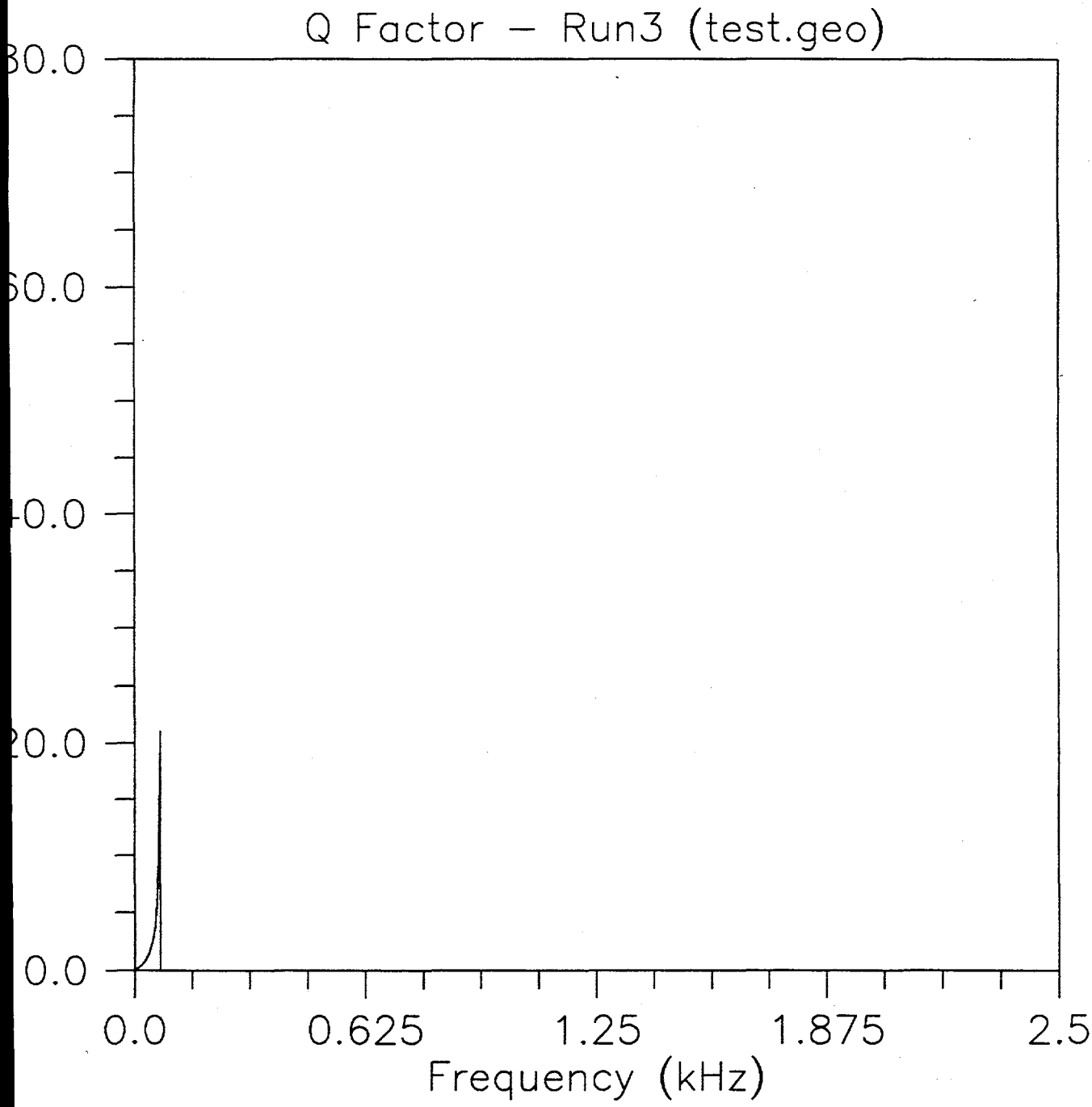
Q Factor – Run3 (test.geo)
80.0
60.0
40.0
20.0
0.0
0.0
0.625
1.25
1.875
2.5
Frequency (kHz)

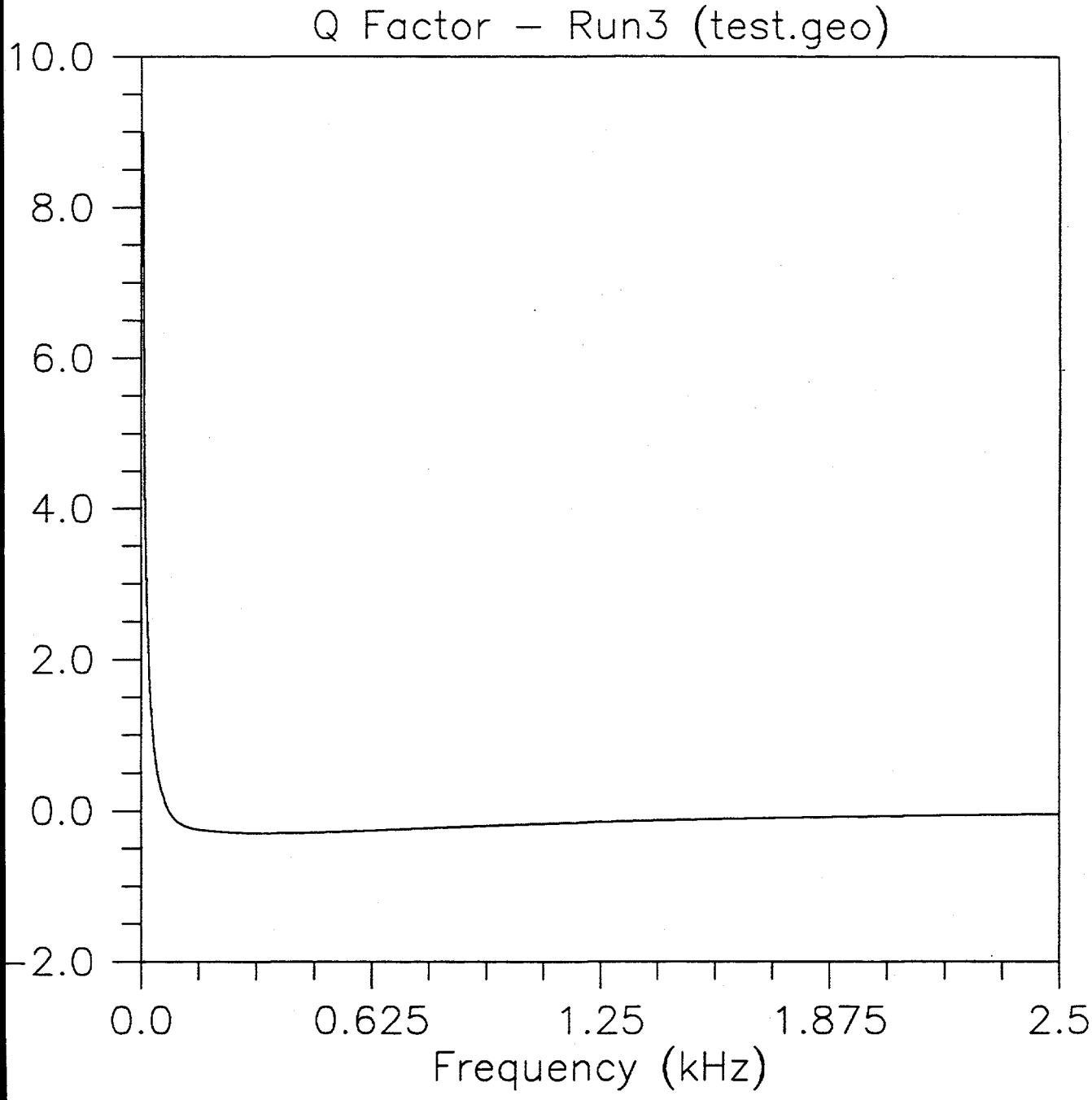
Q Factor – Run3 (test.geo)
10.0
8.0
6.0
4.0
2.0
0.0
-2.0
0.0
0.625
1.25
1.875
2.5
Frequency (kHz)

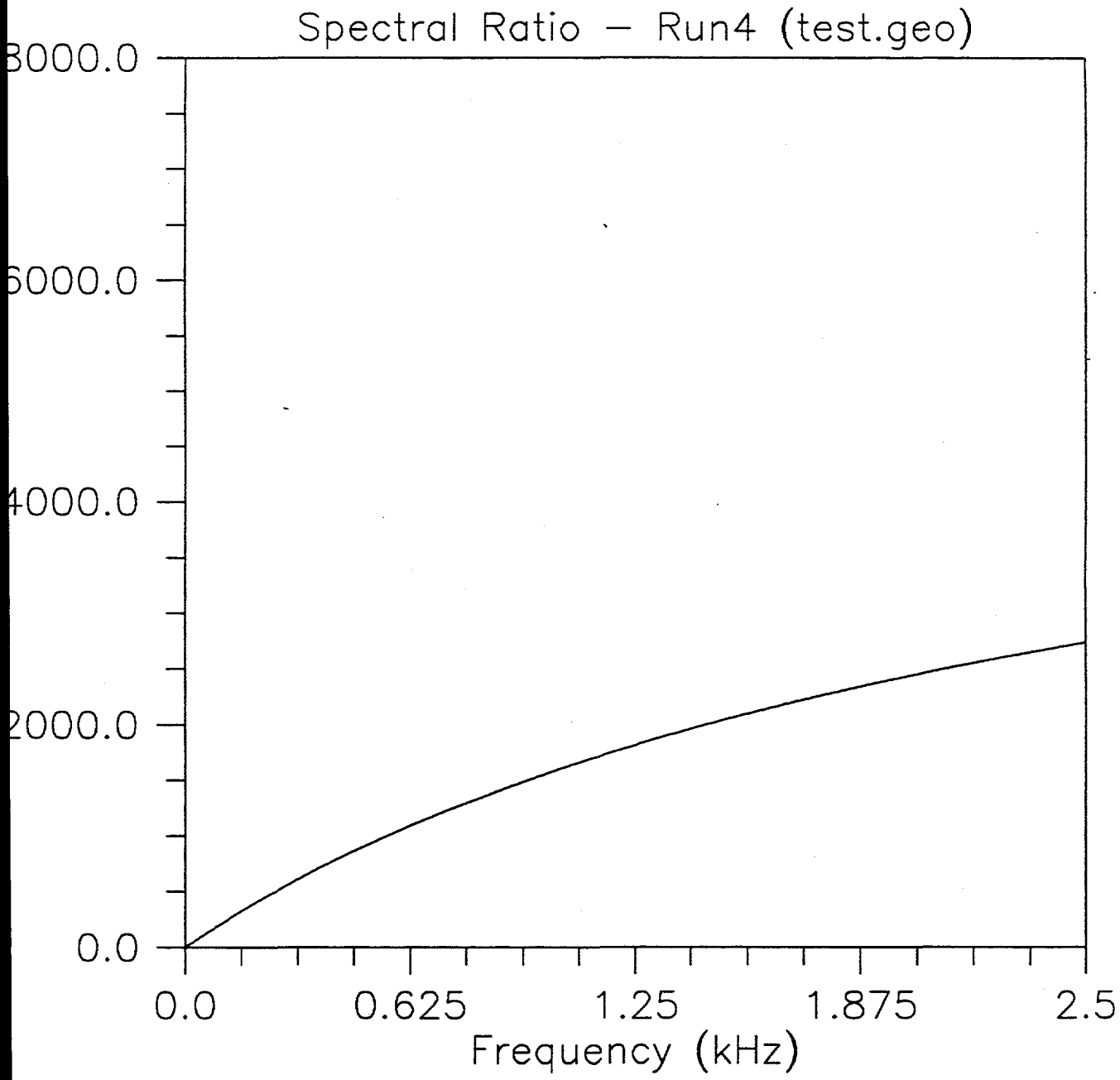
Spectral Ratio – Run4 (test.geo)
8000.0
6000.0
4000.0
2000.0
0.0
0.0
0.625
1.25
1.875
2.5
Frequency (kHz)

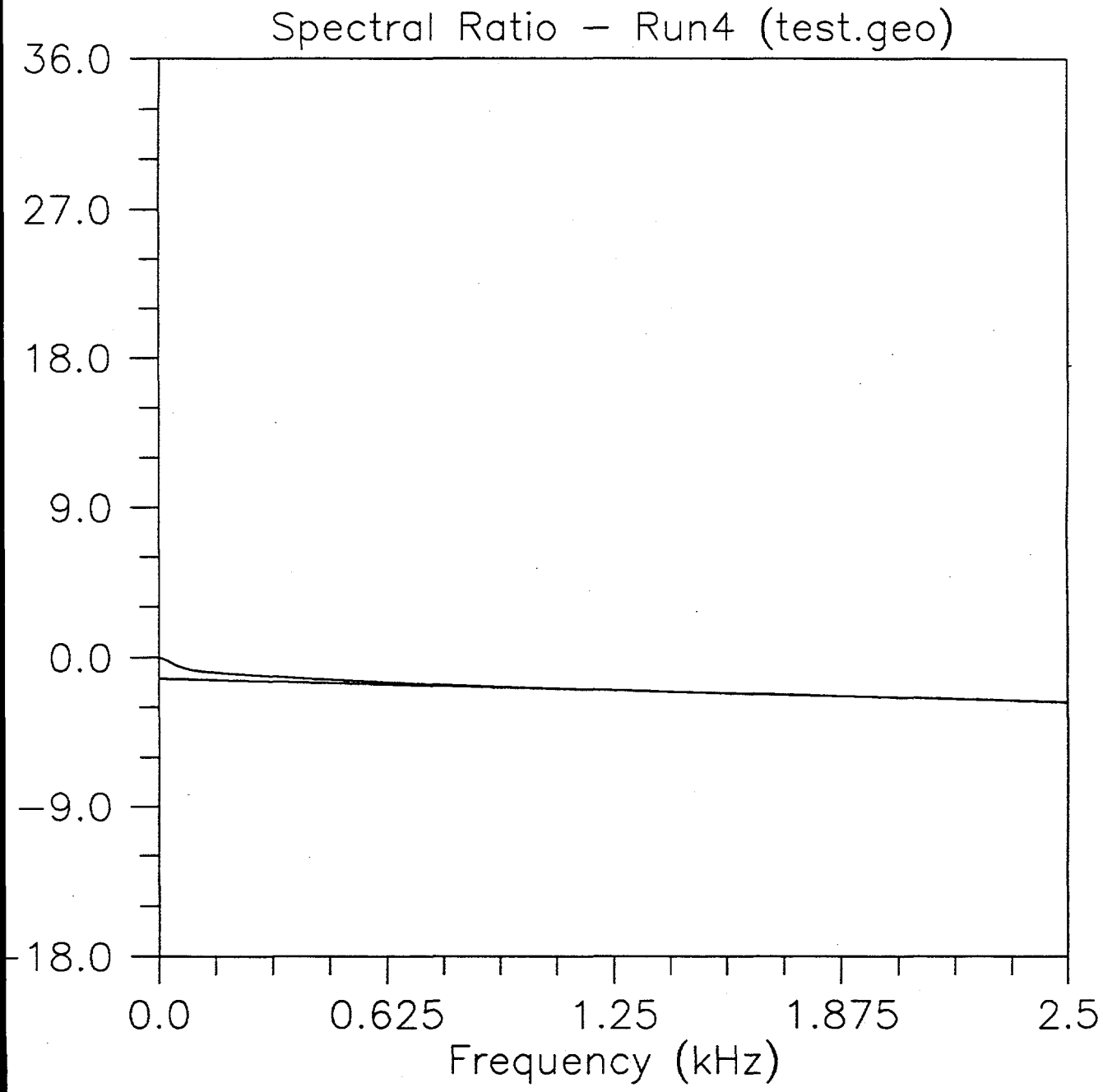
Spectral Ratio – Run4 (test.geo)
36.0
27.0
18.0
9.0
0.0
-9.0
-18.0
0.0
0.625
1.25
1.875
2.5
Frequency (kHz)

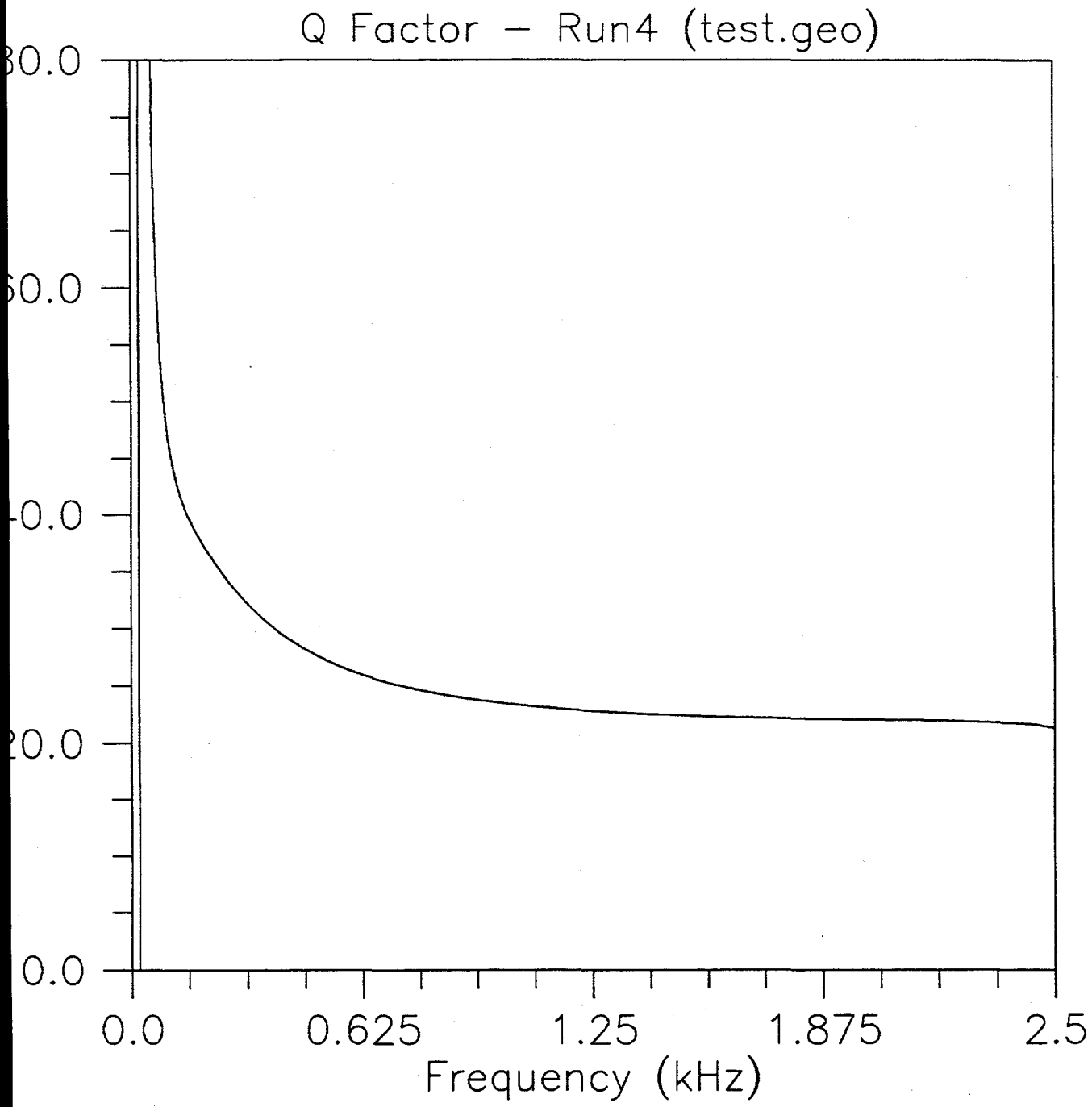
Q Factor – Run4 (test.geo)
80.0
60.0
40.0
20.0
0.0
0.0
0.625
1.25
1.875
2.5
Frequency (kHz)

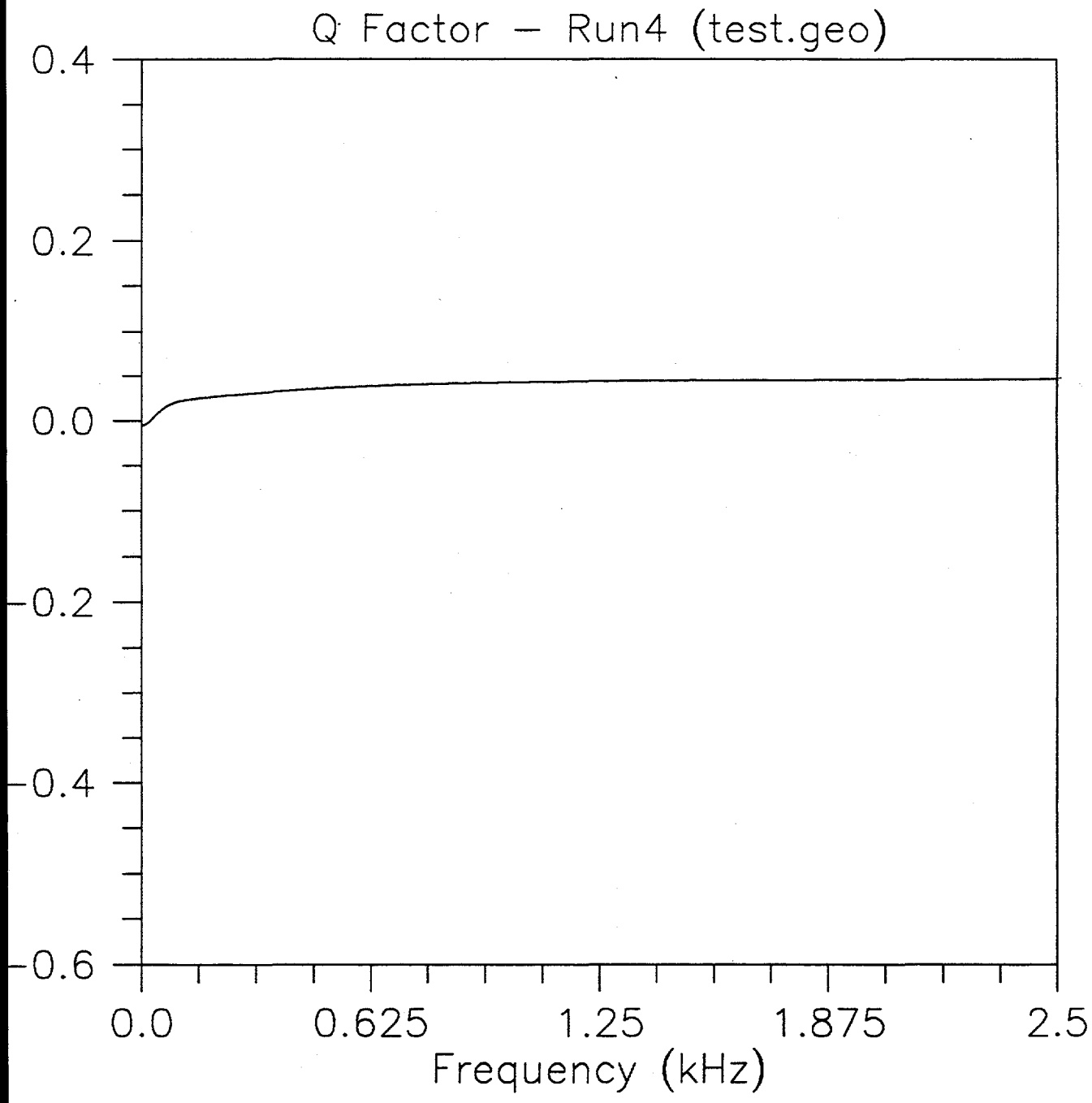
Q Factor – Run4 (test.geo)
0.4
0.2
0.0
-0.2
-0.4
-0.6
0.0
0.625
1.25
1.875
2.5
Frequency (kHz)

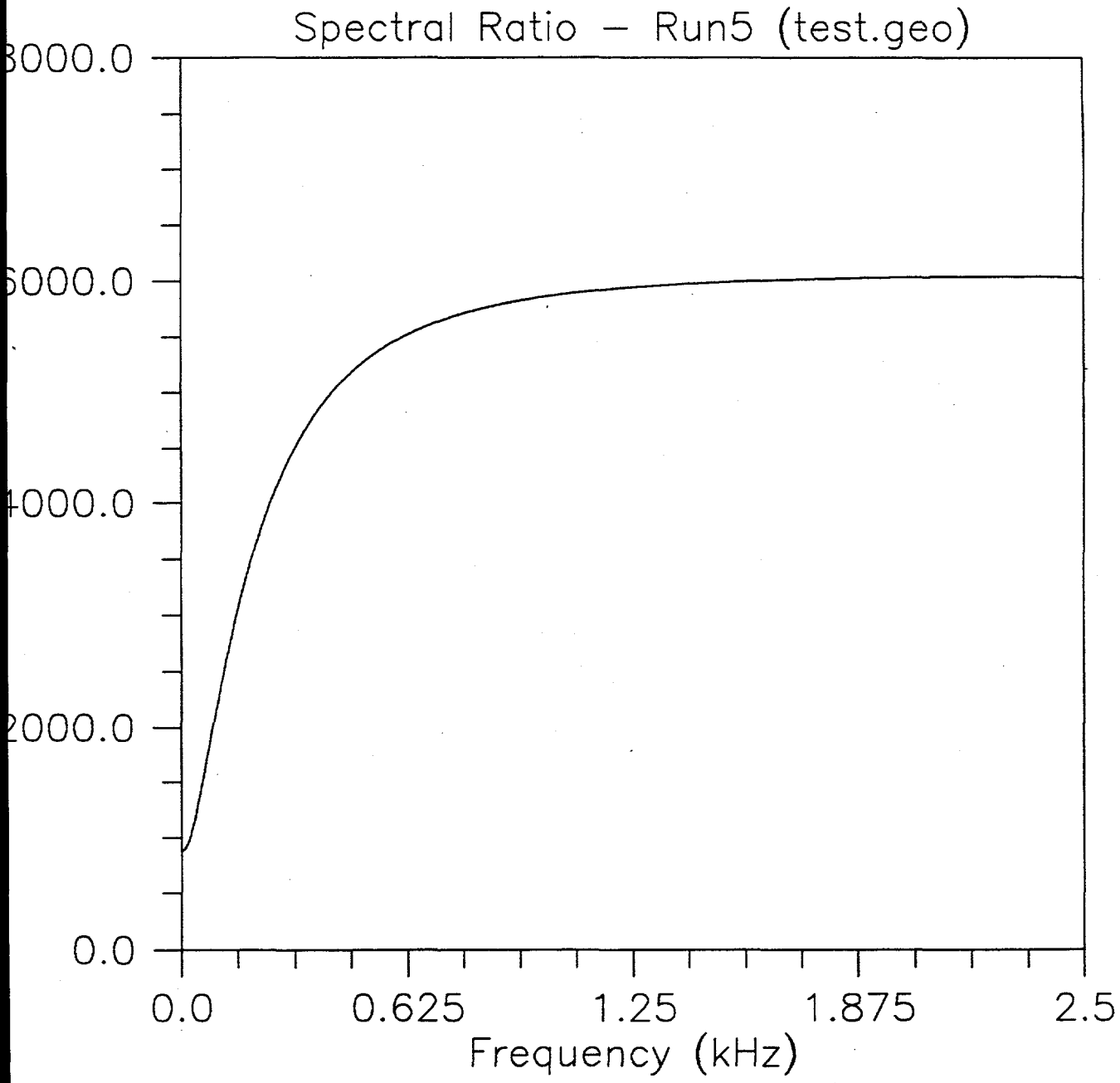
Spectral Ratio – Run5 (test.geo)
8000.0
6000.0
4000.0
2000.0
0.0
0.0
0.625
1.25
1.875
2.5
Frequency (kHz)

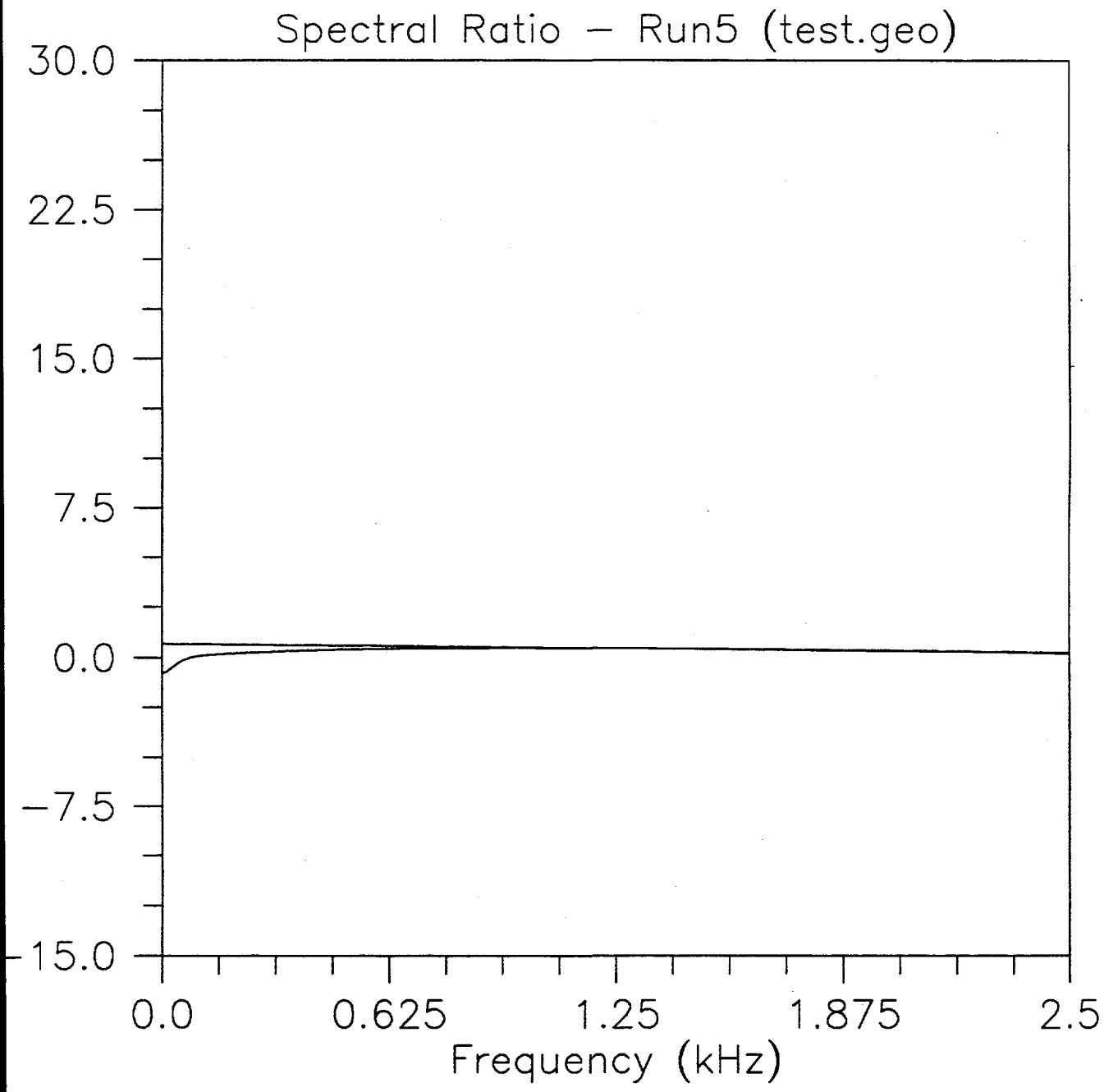
Spectral Ratio – Run5 (test.geo)
30.0
22.5
15.0
7.5
0.0
−7.5
−15.0
0.0
0.625
1.25
1.875
2.5
Frequency (kHz)

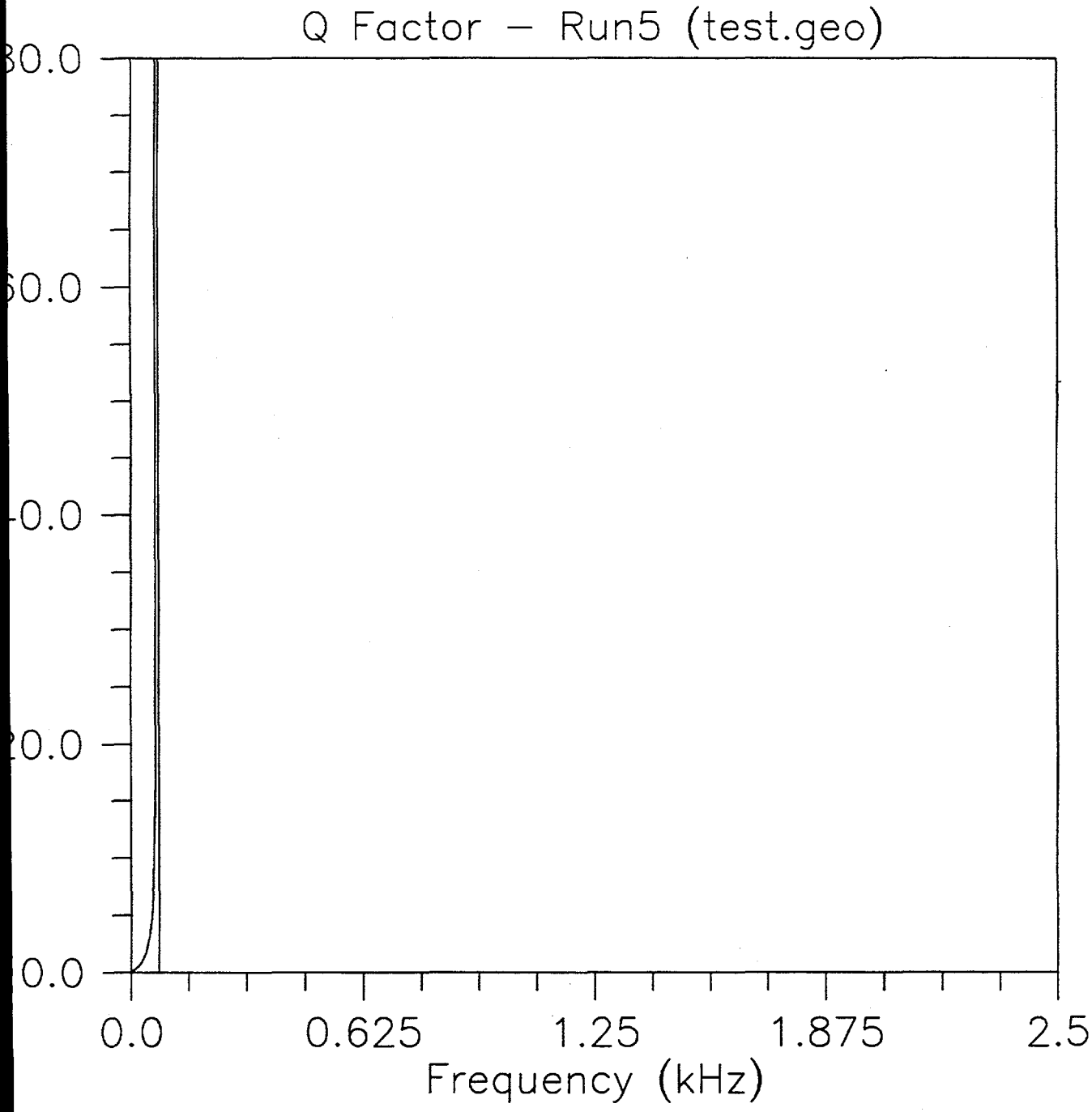
Q Factor – Run5 (test.geo)
80.0
60.0
40.0
20.0
0.0
0.0
0.625
1.25
1.875
2.5
Frequency (kHz)

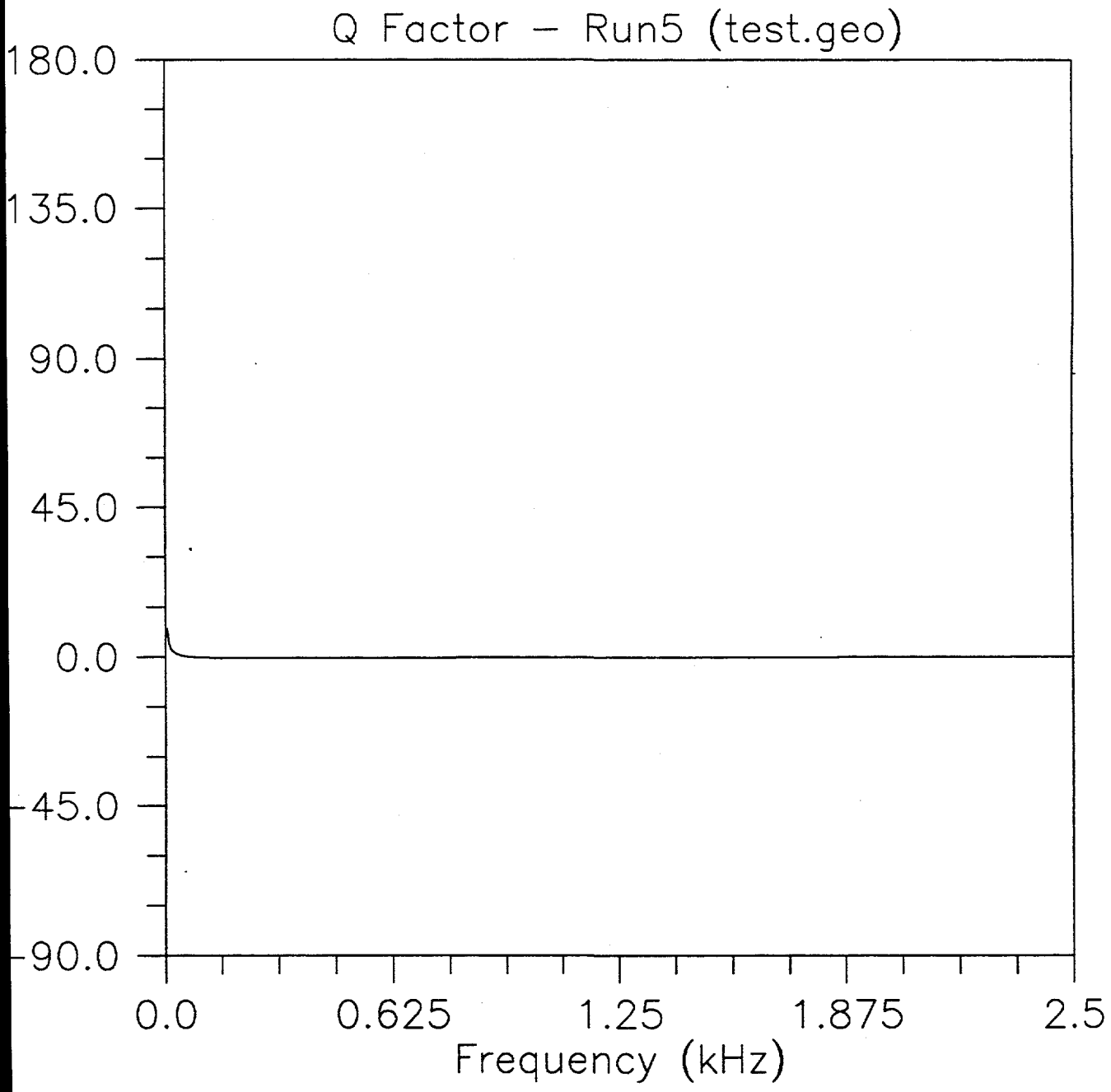
Q Factor – Run5 (test.geo)
180.0
135.0
90.0
45.0
0.0
-45.0
-90.0
0.0
0.625
1.25
1.875
2.5
Frequency (kHz)

APPENDIX C

INTERWELL SEISMIC TRANSMISSION AND REFLECTION THROUGH A DIPPING LOW-VELOCITY LAYER

INTERWELL SEISMIC TRANSMISSION AND REFLECTION THROUGH A DIPPING LOW-VELOCITY LAYER

By

Jorge O. Parra
Vernon R. Sturdivant
Pei-cheng Xu

Southwest Research Institute
6220 Culebra Road
P.O. Drawer 28510
San Antonio, Texas 278228-0510

Received

ABSTRACT

A dipping fractured layer zone has a characteristic seismic signature in interwell seismic data. We simulate a fracture zone as a dipping low-velocity layer in an unbounded medium using the elasto-dynamic Green's function for layered earth to include absorption and dispersion effects. The vector wave displacement solution is developed for a point force at an arbitrary angle with respect to the axis of symmetry of a horizontal layer. The source and detector boreholes are rotated such that the new boreholes are perpendicular to the force to form a new plane which contains a dipping layer and horizontal force. To simulate interwell seismic responses, a modified Clenshaw-Curtis quadrature method for wave number integrals of the Bessel function type is developed to evaluate the wave displacement vector in the frequency-space domain. The model results demonstrate that the presence of a dipping low-velocity layer produces seismic signatures associated with the attitude of the low-velocity layer and the angle of the layer with respect to the source. Also, the results suggest that the amplitudes of shear wave events associated with the presence of a dipping low-velocity layer diminish and their hyperbolic moveout patterns are modified as the dipping layer becomes horizontal.

INTRODUCTION

High-resolution interwell seismic has become an extremely efficient technique for delineating subsurface geological structures and to determine rock physical parameters. In particular, interwell seismic measurements have been used in geophysics to detect fracture zones in granitic rocks applying transmission ray tomography (Wong *et al.*, 1985) and diffraction tomography (Tura, *et al.*, 1992). In order to investigate the applicability of these inversion techniques, synthetic data usually is generated using seismic modeling methods such as finite difference techniques, ray tracing, finite element, and the reflectivity method. However, viscoelastic approximations appear to be more appropriate to represent the earth's seismic response because of the inclusion of absorption and dispersion effects, which are intimately related to lithology (Martinez and McMechan, 1991). The viscoelastic modeling approximation has been used to generate crosswell synthetic seismograms by Jean and Bouchon (1991) to describe the complete wavefield associated with a 3-D source in a multilayer attenuated earth.

In this paper the attenuation characteristics of the media is implemented in the elastodynamic Green's function for layered earth (in the wavenumber domain) following the work of Apsel (1979). Although the complete theoretical analysis for a point force (or pressure source) associated with a multilayered earth is not included in this paper, the explicit vector wave displacement solution is given for a point force in the presence of an attenuated layer in Appendix A. This solution is developed as an application to calculate synthetic seismograms associated with a dipping low-velocity layer which may be used to represent a fracture zone in an unfractured host medium. The characterization and detection of fracture zones have

become important for enhanced oil recovery projects, storage of nuclear toxic waste, and hydrological and geothermal applications. In fact, Tura *et al.* (1992) and Green and Mair (1983) have used seismic wave propagation to detect and characterize fracture zones in granitic rock for radioactive waste disposal sites.

The numerical integration of the Green's function is performed using an effective quadrature scheme with self-adjusting interval length, the Modified Chenshaw-Curtis method. This numerical scheme was developed by Xu and Mal (1985, 1987) and applied by Amundsen and Ursin (1991) to generate synthetic data, which was used as reference data for evaluating a frequency-wavenumber velocity inversion algorithm for surface seismic applications. The Modified Clenshaw-Curtis numerical scheme of integration has been extended to simulate high-resolution interwell seismic logging measurements, and its new elements are in Appendix B.

I. FORMULATION

The basic formulation to derive the Green's function consists of expressing the vector form of the classic elasto-dynamic equation (Kupradze, 1979) in cylindrical coordinates (r, θ, z) and the displacement components in a Fourier series with respect to the azimuth θ. The resulting equations are reduced using the Hankel transform method to produce a set of two-coupled partial differential equations associated with compressional waves and vertical polarized shear waves, and a separate partial differential equation associated with SH-waves. Solutions of these partial differential equations yield the vector wave displacement components for a point force in an infinite elastic medium.

A. Equation of Motion

General solutions of the inhomogeneous equations of motion for a uniform isotropic viscoelastic medium are derived. The equations of motion in cylindrical coordinates (r, θ, z) assuming exp (−jωt) variation are

$$\begin{aligned}
&\mu\left[\nabla^2 u_r - \frac{1}{r}\left(2\frac{\partial u_\theta}{r\partial\theta} + \frac{u_r}{r}\right)\right] + (\lambda+\mu)\frac{\partial\Delta}{\partial r} + \omega^2\rho u_r + F_r = 0\,,\\
&\mu\left[\nabla^2 u_\theta - \frac{1}{r}\left(\frac{u_\theta}{r} - \frac{\partial u_r}{r\partial\theta}\right)\right] + (\lambda+\mu)\frac{\partial\Delta}{r\partial\theta} + \omega^2\rho u_\theta + F_\theta = 0\,,\\
&\mu\nabla^2 u_z + (\lambda+\mu)\frac{\partial\Delta}{\partial z} + \omega^2\rho u_z + F_z = 0\,,
\end{aligned} \tag{1}$$

in which (u_r, u_θ, u_z) and (F_r, F_θ, F_z) correspond to the components of the displacement and body force per unit volume in the r, θ, and z directions, respectively. The Lamé constants (which may be complex) are denoted by λ and μ, while the density and the frequency are

represented by ρ and ω, respectively. In the equations above, ∇^2 represents the Laplacian operator, while Δ denotes the dilatation.

B. Equation of Motion in the Wave Number Domain

Expanding the displacement and body force in a Fourier series with respect to the azimuth θ, a system of equations is obtained in terms of the vector displacement (u_{rn}, $u_{\theta n}$, u_{zn}) and the body force (F_{rn}, $F_{\theta n}$, F_{zn}) wave coefficients. This resulting system of equations is reduced (in the wave number domain) using the Hankel transform method to one set of two coupled partial differential equations and a separate uncoupled partial differential equation. In the wave number domain, k, the coupled system of differential equations is given by

$$\left[\mu\frac{d^2}{dz^2} - (\lambda + 2\mu)k^2 + \omega^2\rho\right]u_{1n} - k(\lambda + \mu)\frac{du_{2n}}{dz} + F_{1n} = 0, \tag{2a}$$

$$-k(\lambda + \mu)\frac{du_{1n}}{dz} - \left[(\lambda + 2\mu)\frac{d^2}{dz^2} - \mu k^2 + \omega^2\rho\right]u_{2n} - F_{2n} = 0, \tag{2b}$$

and the uncoupled partial differential equation is given by

$$\left[\mu\frac{d^2}{dz^2} - \mu k^2 + \omega^2\rho\right]u_{3n} + F_{3n} = 0. \tag{3}$$

The functions $u_{1n}(z,k)$ and $u_{2n}(z,k)$ are coupled through Eqs. (2a) and (2b) and are independent of $u_{3n}(z,k)$ which must satisfy Eq. (3). The functions u_{1n} and u_{2n} are associated with compressional waves and vertical polarized shear waves. The function $u_{3n}(z,k)$ in Eq. (3) is associated with waves whose particle motion is polarized in horizontal plane.

C. The Green's Function

The coupled system of partial differential equations given by Eq. (2) can be expressed as

$$\mathfrak{L}u = F, \tag{4}$$

where $u = \begin{pmatrix} u_{1n} \\ u_{2n} \end{pmatrix}$, and $F = \begin{pmatrix} -F_{1n} \\ F_{2n} \end{pmatrix}$; for $n = 1, 2$.

$\mathfrak{L}$ is the differential operator of components $\mathfrak{L}_{ij}$ given by

$$\mathfrak{L}_{ij} = \begin{bmatrix} \left[\mu\frac{d^2}{dz^2} - (\lambda+2\mu)k^2 + \omega^2\rho\right] & -k(\lambda+\mu)\frac{d}{dz} \\ -k(\lambda+\mu)\frac{d}{dz} & -\left[(\lambda+2\mu)\frac{d^2}{dz^2} - \mu k^2 + \omega^2\rho\right] \end{bmatrix}. \tag{5}$$

Since the Green's function for a point force in an unbounded medium is given in Apsel (1979), only the final expression for the vector wave displacement is presented. Thus, displacement components in directions *i* due to a horizontal point force $f_1(\omega)$ and a vertical point force $f_2(\omega)$ are given by

$$u_{ij} = \begin{pmatrix} -k & \chi \\ -\nu & k \end{pmatrix} \begin{pmatrix} \frac{k}{\nu}e^{-\nu(z-z_s)} & e^{-\nu(z-z_s)} \\ e^{-\chi(z-z_s)} & \frac{k}{\chi}e^{-\chi(z-z_s)} \end{pmatrix} \begin{pmatrix} f_1(\omega) & 0 \\ 0 & f_2(\omega) \end{pmatrix}; \tag{6}$$

for $j = 1, 2$ and $i = 1, 2$,

where (r, θ, z) is the detector coordinate and $(0, 0, z_s)$ is the source position. The wave parameters ν and χ are given by

$$u_r = -\frac{F(\omega)}{4\pi\rho_3\omega^2}\sin\delta\cos\theta\int_0^\infty u_{11}(k)kJ_0(kr)dk$$

$$+\frac{F(\omega)}{4\pi\rho_3\omega^2}\int_0^\infty\left\{\frac{1}{r}\left[u_{11}(k)+k_s^{(3)^2}u_{31}(k)\right]\sin\delta\cos\theta\right. \tag{9a}$$

$$\left.+u_{10}(k)k\cos\delta\right\}J_1(kr)dk,$$

$$u_\theta = u_\theta^{(h)}, \tag{9b}$$

and

$$u_z = \frac{F(\omega)}{4\pi\rho_3\omega^2}\int_0^\infty\left[-\sin\delta\cos\theta\,u_{21}(k)+\cos\delta\,u_{10}(k)\right]kJ_1(kr)dk. \tag{9c}$$

We have selected the source position (r_s, θ_s, z_s) as the origin of the cylindrical coordinate system (r, θ, z). To simplify the solution of a horizontal layer in an unbounded medium, we assumed that source and detector boreholes are contained in the vertical rz-plane for $\theta = 0°$. In addition, to simulate the interwell seismic response for a horizontal point force in the presence of a dipping layer, we consider a r′z′-plane containing new source and detector boreholes and a horizontal force as shown in Fig. 1. The r′z′-plane is oriented at an angle $\gamma = 90°-\delta$ with respect to the vertical rz-plane which contains the horizontal layer and the force F (oriented at an angle δ with respect to the z-axis of symmetry). In the r′z′-plane a dipping layer is observed by sensors placed in the borehole oriented in the z′-direction. Therefore, the displacement components measured by detectors oriented parallel and

perpendicular to the detector borehole in the z′-direction, may be derived by rotating the displacement components, given by Eqs. (9a) and (9c), as follows:

$$u_z' = u_r \cos\delta + u_z \sin\delta \tag{10a}$$

and

$$u_r' = u_r \sin\delta - u_z \cos\delta \,. \tag{10b}$$

The coordinates at a given detector position above the layer in the new receiver borehole are given by

$$r = z_d \frac{\cos\delta}{\sin\delta} + b/\sin\delta\,;\ \text{for}\ \delta > 0 \tag{11a}$$

and

$$z = z_d\,, \tag{11b}$$

where

b = borehole separation

and z_d = detector position in the old system.

The numerical evaluation of the wavenumber integrals of highly irregular and oscillatory functions given in Eqs. (9a), (9b), and (9c) was accomplished using a modified and extended version of the Clenshaw-Curtis method which is given in the Appendix B. The vector displacement time response in terms of the borehole separation r and the angle δ was obtained numerically using FFT.

II. NUMERICAL EXAMPLES

The primary application of the present solution is to model the seismic response of a dipping low-velocity layer with respect to a pair of transmitter and receiver boreholes. However, seismic responses of a source in an unbounded medium and a source in the presence of a horizontal low-velocity layer are required as reference model responses to thoroughly analyze the dipping layer case. Thus, seismic responses were calculated for an earth model consisting of a horizontal low-velocity layer of thickness 5 m in an unbounded host medium as shown in Fig. 2. The physical properties of this model are given in Table I. The source pulse signal was assumed to be a nonzero phase Ricker wavelet. The horizontal and vertical displacements synthetic seismograms for a horizontal force pulse signal centered at f_o = 500 Hz were calculated at twelve different detector positions for the model shown in Fig. 2. The horizontal point source was located at the source depth of 5 m below the layer, and detectors were located at a horizontal distance of 35 m from the source. The two component detectors were spaced 7.5 m apart above the layer, in the layer, and below the layer.

Figures 3a and 3b illustrate the horizontal and vertical displacement seismograms for the model of Fig. 2, and the Figs. 3c and 3d show the corresponding seismograms associated with the horizontal force in the absence of the layer. Comparisons between these seismograms show that the P-wave and S-wave events observed by detectors above the layer arrive approximately 2 ms later than the corresponding events observed in the full space seismograms. In addition, small reflection amplitudes are observed by detectors below the layer, and multiple reflections are observed by detectors located within the low-velocity layer. These observations appear to be better analyzed using hodogram plots. In fact, to

characterize a low-velocity layer in the presence of a point source (force) in more detail, synthetic seismograms given in Figs. 3 were used to produce polarization diagrams (hodograms) which were made by plotting one detector component along the horizontal axis and plotting the other component along the vertical axis and are presented for selected time windows.

Figures 4 and 5 illustrate the time-variant signal hodograms produced from the synthetic seismograms given by Figs. 3. Since each hodogram was constructed using a full trace (i.e., 0–50 ms), most of them exhibit both lobes, a P-wave lobe pointing to the source and an S-wave to be perpendicular to the P-wave lobe. The resulting hodogram plots show small rotations associated with the time-delay observed by detectors above the layer. These small rotations are due to the slight difference in the transmission coefficients from the high-to-low and low-to-high impedance boundaries. On the other hand, the particle motions are almost linear at detector positions below the source because the polarization radiated from the source is preserved as shear waves penetrate an isotropic medium. However, the polarization diagram observed by the detector located within the low-velocity layer shows a complicated pattern associated with the multiple reflections and interaction between the different types of reflections coefficients. As a consequence, we investigated this wavefield characteristic by constructing hodogram plots using different time windows. Since the S-wave events are sensitive to the presence of the low-velocity layer, we illustrate the shear wave events associated with the detector within the layer. The corresponding hodograms are presented for time windows of 15–21 ms and 21–28 ms in Figs. 6a and 6b, respectively. In particular, the hodogram produced using a time window between 15–21 ms appears 90 percent rotated with respect to the corresponding S-wave event in the absence of the layer.

The response of a low-velocity layer dipping 40 degrees with respect to the horizontal separation between source and detector boreholes is calculated using Eqs. 23. The geometry of this dipping layer which includes the source and detector locations is illustrated in Fig. 7, and the physical properties of the model are given in Table I. Horizontal and vertical displacement seismograms for this dipping layer in the presence of a horizonal point force are shown in Figs. 8a and 8d together with the corresponding seismograms associated with a horizontal point force in the unbounded medium. The time of arrivals of the waveforms calculated at detectors positions above the layer exhibit time delays relative to the unbounded medium waveforms. In addition, the seismic waveforms are overlapped and distorted when detectors are placed above and within the layer, and between the layer and the seismic source. Thus, to characterize these waveforms, the shear wave events are displayed as polarization diagram plots in Figs. 9a and 9b.

The polarization plots produced from waveforms calculated at detectors positions 1, 2, 3, and 4 (see Figs. 9a and 9b) show characteristic signatures associated with the presence of a dipping layer. The field radiated by the source has been rotated and modified by the presence of the low-velocity layer. In particular, the wavefield observed at the detector position within the layer has been rotated 90 degrees, and the wavefield observed at detectors placed below the layer exhibit a type of split polarization. In fact, the wavefield observed at the detector position immediately below the layer becomes distorted as a result of the difference in reflection coefficients between SV- and SH-waves at the interface. These reflection coefficients may cause phase changes between reflected SV- and SH-components producing effects very similar to shear-wave splitting, with a resulting change in polarization of the reflected waves

at the low-velocity layer interface (Yardey and Crampin, 1991). However, the wavefields calculated at detectors below the source are less distorted and follow the same patterns of those wavefields radiated by the source in an unbounded medium.

The effects of split polarization discussed above have been observed when the source has a dominant frequency of 500 Hz and radiates shear waves having wavelengths less than or equal to the layer thickness for the model given in Fig. 7. The polarization plots shown in Fig. 10 demonstrate that these effects of split polarization are diminished as the source peak frequency is reduced to 300 Hz. The corresponding horizontal and vertical displacement seismograms show losses in the characteristic signatures associated with the layer thickness by displaying 300 Hz pulse waveforms in Fig. 11. Although wave features related to the layer thickness have been reduced in the synthetic seismic traces, the second reflection-converted and transmitted-converted shear wave events remain in the seismograms. These shear wave events are directly related to the presence of the dipping layer since they are absent for the case of the horizontal layer in an unbounded medium as shown in Figs. 3a and 3b. We expect that the amplitudes of these shear wave events will be diminished and their hyperbolic moveout patterns will be modified in the seismograms as the dipping layer becomes horizontal.

III. CONCLUSIONS

Explicit vector wave displacement components have been derived to calculate the response of a dipping layer in an unbounded medium near a point force. The Modified Clenshaw-Curtis method of integration was extended to evaluate high-oscillatory kernels associated with high-resolution three-dimensional applications. The model responses demonstrate that the presence of a dipping layer can be inferred by analyzing multicomponent seismograms and shear-wave polarization diagrams constructed from waveforms at different detector positions in the borehole. Seismic waveforms calculated at detectors located between the source and the low-velocity layer produces characteristic signatures associated with the attitude and angle of the layer with respect to the boreholes. The analytical vector wave displacement solution can be easily generalized to simulate the response of a dipping multilayer structure with respect to the boreholes to calculate interwell seismograms for high-resolution applications. In addition, the Green's function for transversely isotropic layered formations can be implemented and evaluated using the Modified Clenshaw-Curtis method of integration for high-oscillatory integrals.

Abramowitz, M. and Stegun, I. A., 1972, *Handbook of Mathematical Functions*, Dover, New York, pp. 253–294.

Amundsen, L. and Ursin, B., 1991, "Frequency-wavenumber inversion of acoustic data," *Geophysics*, **56**, 1027–1039.

Apsel, R. J., 1991, "Dynamic Green's function for layered media and applications to boundary value problems," Ph.D. thesis, University of California at San Diego, La Jolla, California.

Dravinski, M. and Mossessian, T. K., 1988, "On evaluation of the Green functions for harmonic line loads in a viscoelastic half space," *Int. J. for Num. Methods in Eng.*, **26**, pp. 823–841.

Futterman, W. I., 1962, "Dispersive body waves," *Journal Geophysical Research*, **67**, 5279–5291.

Gradshteyn, I. S. and Ryzhik, I., 1980, *Table of Integrals, Series, and Products*, Academic Press, pp. 681–720, 940–942.

Green, A. G. and Mair, J. A., 1983, "Subhorizontal fractures in a granitic pluton: Their detection and implications for radioactive waste disposal," *Geophysics*, **48**, pp. 1428–1449.

Hitchcock, A. J. M., 1957, "Polynomial approximation to Bessel functions of order zero and one and to related functions," *Mathematical Table and Other Aids to Computation*, **XI**(57–60), pp. 86–88.

Jean, P. and Bouchon, J., 1991, "Cross-borehole simulation of wave propagation," *Geophysics*, **56**, pp. 1103–1113.

Kupradze, V. D., 1979, "The three-dimensional problems of the mathematical theory of elasticity and thermoelasticity," North-Holland, Amsterdam.

Martinez, R. D. and McMechan, G. A., 1991, "τ-P seismic data for viscoelastic media—Part 1: modeling," *Geophysical Prospecting*, **39**, pp. 141–156.

Parra, J. O., 1991, "Analysis of elastic wave propagation in stratified fluid-filled porous media for interwell seismic applications," *Journal of the Acoustical Society of America*, **90**, pp. 2557–2878.

Tura, M. A. C., Johnson, L. R., Majer, E. L., and Peterson, J. E., 1992, "Application of diffraction tomography to fracture detection," *Geophysics*, **57**, pp. 245–257.

Wong, J., Hurley, P., and West, G. F., 1984, "Crosshole audiofrequency seismology in granitic rocks using piezoelectric transducers as sources and detectors," *Geoexploration*, **22**, pp. 261–279.

Xu, P.-C. and Mal, A. K., 1985, "An adaptive integration scheme for irregularly oscillatory functions," *Wave Motion*, 7, pp. 235–243.

Xu, P.-C. and Mal, A. K., 1987, "Calculation of the inplane Green's functions for layered solids," *Bull. Seism. Soc. Am.*, **77**(4), pp.-1823–1837.

APPENDIX A: VECTOR DISPLACEMENT SOLUTIONS FOR HORIZONTAL AND VERTICAL POINT FORCES

The particle displacements in the j^{th} elastic medium associated with compressional and vertical polarized shear waves are:

For a horizontal point force (n = 1):

$$\begin{pmatrix} u_{11}^{(j)} \\ u_{21}^{(j)} \end{pmatrix} = \begin{bmatrix} -k & \chi_j \\ -\nu_j & k \end{bmatrix} \begin{pmatrix} e^{-\nu_j(z-z_{j-i})} & 0 \\ 0 & e^{-\chi_j(z-z_{j-1})} \end{pmatrix} \begin{pmatrix} \eta_1^{(j)} \\ \eta_2^{(j)} \end{pmatrix}$$

$$+ \begin{bmatrix} -k & \chi_j \\ \nu_j & -k \end{bmatrix} \begin{pmatrix} e^{\nu_j(z-z_j)} & 0 \\ 0 & e^{\chi_j(z-z_j)} \end{pmatrix} \begin{pmatrix} \eta_3^{(j)} \\ \eta_4^{(j)} \end{pmatrix}; \qquad \text{(A-1)}$$

and $$u_{31}^{(j)} = \eta_5^{(j)} e^{-\chi_j(z-z_{j-1})} + \eta_6^{(j)} e^{\chi_j(z-z_j)}; \text{ for } z_{j-1} < z < z_j, \qquad \text{(A-2)}$$

where $\eta_i^{(j)}$ (for i = 1, 4) are wave functions expressed in terms of generalized reflection and transmission matrices associated with P and SV waves. Alternatively, the wave functions $\eta_5^{(j)}$ and $\eta_6^{(j)}$ are associated with SH-waves.

For a vertical point force (n = 0):

$$\begin{pmatrix} u_{10}^{(j)} \\ u_{20}^{(j)} \end{pmatrix} = \begin{bmatrix} -k & \chi_j \\ -\nu_j & k \end{bmatrix} \begin{pmatrix} e^{-\nu_j(z-z_{j-i})} & 0 \\ 0 & e^{-\chi_j(z-z_{j-1})} \end{pmatrix} \begin{pmatrix} \Omega_1^{(j)} \\ \Omega_2^{(j)} \end{pmatrix}$$

$$+ \begin{bmatrix} -k & \chi_j \\ \nu_j & -k \end{bmatrix} \begin{pmatrix} e^{\nu_j(z-z_j)} & 0 \\ 0 & e^{\chi_j(z-z_j)} \end{pmatrix} \begin{pmatrix} \Omega_3^{(j)} \\ \Omega_4^{(j)} \end{pmatrix}; \qquad \text{(A-3)}$$

$$\text{for } z_{j-1} < z < z_j,$$

where $\Omega_i^{(j)}$ (for i = 1, 4) are also wave functions expressed in terms of generalized reflection and transmission matrices formed by coefficients associated with P-waves and SV-waves.

The source transmits seismic pulses at the source depth $z_s^{(m)}$, and measurements are recorded at detectors depths $z^{(j)}$; for j = m − 2 = 1, 2,... N, where N is the number of layers in the formation and m is the layer containing the source. As an example, we present the solution for a layered earth model in which the source is in the bottom half-space (m = 3) and the detectors are in the first layer (j = 1). Thus, the wave functions $\eta_i^{(1)}$ (for i = 1, 4) associated with a horizontal force (n = 1) are given by

$$\begin{pmatrix} \eta_1^{(1)} \\ \eta_2^{(1)} \end{pmatrix} = \hat{R}_o^{\,u}\, \hat{T}_1^{\,u}\, \hat{T}_2^{\,u}\, S_{u1}^{(3)} \qquad \text{(A-4)}$$

$$\begin{pmatrix} \eta_3^{(1)} \\ \\ \eta_4^{(1)} \end{pmatrix} = \hat{T}_1^{\,u}\ \hat{T}_2^{\,u}\ S_{u1}^{(3)}; \tag{A-5}$$

where $S_{u1}^{(3)}$ is the source function given by

$$S_{u1}^{(3)} = \begin{pmatrix} \dfrac{k}{\nu_3} e^{-\nu_3(z_s - z_3)} \\ \\ e^{-\chi_3(z_s - z_3)} \end{pmatrix}. \tag{A-6}$$

$\hat{T}_1^{\,u}$, $\hat{T}_2^{\,u}$, and $\hat{R}_o^{\,u}$ are generalized 2×2 transmission and reflection matrices, which are obtained recursively from the modified transmission and reflection matrices of coefficients given in Apsel (1979).

After substituting Eq. (A-6) into Eqs. (A-4) and (A-5), the resulting wave functions $\eta_i^{(1)}$ are expanded in terms of products of transmission and reflection matrix coefficients. The new wave functions $\eta_i^{(1)}$ are substituted into Eq. (A-1) to yield the vector displacement in the wavenumber domain associated with P-waves and SV-waves:

$$u_{11} = -k\, e^{-\nu_1 z}\left[q_{11} \frac{k}{\nu_3} e^{-\nu_3(z_s - z_2)} + q_{12}\, e^{-\chi_3(z_s - z_2)} \right]$$

$$+ \chi_1\, e^{-\chi_1 z}\left[q_{21} \frac{k}{\nu_3} e^{-\nu_3(z_s - z_2)} + q_{22}\, e^{-\chi_3(z_s - z_2)} \right]$$

$$-k\, e^{-\nu_1(z_1 - z)}\left[p_{11} \frac{k}{\nu_3} e^{-\nu_3(z_s - z_2)} + p_{12}\, e^{-\chi_3(z_s - z_2)} \right]$$

$$+\chi_1 e^{-\chi_1(z_1-z)}\left[p_{21}\frac{k}{\nu_3}e^{-\nu_3(z_s-z_2)}+p_{22}e^{-\chi_3(z_s-z_2)}\right] \qquad \text{(A-7a)}$$

$$u_{21} = -\nu_1 e^{-\nu_1 z}\left[q_{11}\frac{k}{\nu_3}e^{-\nu_3(z_s-z_2)}+q_{12}e^{-\chi_3(z_s-z_2)}\right]$$

$$+k e^{-\chi_1 z}\left[q_{21}\frac{k}{\nu_3}e^{-\nu_3(z_s-z_2)}+q_{22}e^{-\chi_3(z_s-z_2)}\right]$$

$$+\nu_1 e^{-\nu_1(z_1-z)}\left[p_{11}\frac{k}{\nu_3}e^{-\nu_3(z_s-z_2)}+p_{12}e^{-\chi_3(z_s-z_2)}\right]$$

$$-k e^{-\chi_1(z_1-z)}\left[p_{21}\frac{k}{\nu_3}e^{-\nu_3(z_s-z_2)}+p_{22}e^{-\chi_3(z_s-z_2)}\right], \qquad \text{(A-7b)}$$

where $q_{ij} = \left[\hat{R}_o^{\,u}\hat{T}_1\hat{H}_2^{\,u}\right]$,

and $p_{ij} = \left[\hat{T}_1\hat{H}_2\right]$; for i,j = 1,2.

The definition of the generalized transmission matrix $\hat{H}_2$ is given in Parra (1991). The wave functions $\eta_5^{(1)}$ and $\eta_6^{(1)}$ associated with SH-waves are also determined and substituted into Eq. (A-2) to yield the displacement component in the wavenumber domain

$$u_{31} = \frac{e^{-\chi_3(z_s-z_2)}}{\chi_3}\left[p_{SH}e^{-\chi_1(z_1-z)}+q_{SH}e^{-\chi_1 z}\right], \qquad \text{(A-8)}$$

where $p_{SH} = \left[\hat{R}_o^{\,u}\,\hat{T}_1\,\hat{H}_2\right]_{SH}$,

and $q_{SH} = \left[\hat{T}_1\,\hat{H}_2\right]_{SH}$.

In a similar fashion, the vector displacement may be derived for a vertical point force (n = 0) with the exception that the source function is given by

$$S_{u0}^{(3)} = -\begin{pmatrix} e^{-\nu_3(z_s - z_2)} \\ \dfrac{k}{\chi_3}\, e^{-\chi_3(z_s - z_2)} \end{pmatrix}.$$

Thus, the displacement components in terms of the products of tramission and reflection coefficients, p_{ij} and q_{ij}, are given by

$$\begin{aligned} u_{10} = -\Bigg\{ & -k\, e^{-\nu_1 z}\left[q_{11}\, e^{-\nu_3(z_s - z_2)} + q_{12}\frac{k}{\chi_3}\, e^{-\chi_3(z_s - z_2)} \right] \\ & + \chi_1\, e^{-\chi_1 z}\left[q_{21}\, e^{-\nu_3(z_s - z_2)} + q_{22}\frac{k}{\chi_3}\, e^{-\chi_3(z_s - z_2)} \right] \\ & - k\, e^{-\nu_1(z_1 - z)}\left[p_{11}\, e^{-\nu_3(z_s - z_2)} + p_{12}\frac{k}{\chi_3}\, e^{-\chi_3(z_s - z_2)} \right] \\ & + \chi_1\, e^{-\chi_1(z_1 - z)}\left[p_{21}\, e^{-\nu_3(z_s - z_2)} + p_{22}\frac{k}{\chi_3}\, e^{-\chi_3(z_s - z_2)} \right] \Bigg\} \end{aligned} \qquad \text{(A-9a)}$$

and

$$u_{20} = -\Bigg\{-\nu_1 e^{-\nu_1 z}\left[q_{11} e^{-\nu_3(z_s - z_2)} + q_{12}\frac{k}{\chi_3} e^{-\chi_3(z_s - z_2)}\right]$$

$$+ k e^{\chi_1 z}\left[q_{21} e^{-\nu_3(z_s - z_2)} + q_{22}\frac{k}{\chi_3} e^{-\chi_3(z_s - z_2)}\right]$$

$$+ \nu_1 e^{-\nu_1(z_1 - z)}\left[p_{11} e^{-\nu_3(z_s - z_2)} + p_{12}\frac{k}{\chi_3} e^{-\chi_3(z_s - z_2)}\right]$$

$$- k e^{-\chi_1(z_1 - z)}\left[p_{21} e^{-\nu_3(z_s - z_2)} + p_{22}\frac{k}{\chi_3} e^{-\chi_3(z_s - z_2)}\right]\Bigg\}. \qquad \text{(A-9b)}$$

The frequency domain solution of the vector displacement $\left(u_r, u_\theta, u_z\right)$ observed in the detector position (r, θ, z) associated with a horizontal point force (n = 1) at a source depth $z_s \equiv z_s^{(3)}$ for the horizontal source-detector separation r is given by

$$u_r^{(h)} = -\frac{F_r(\omega)}{4\pi\rho_3\omega^2}\cos\theta\int_0^\infty u_{11}(k)\,k J_0(kr)\,dk$$

$$+\frac{F_r(\omega)}{4\pi\rho_3\omega^2}\cos\theta\,\frac{1}{r}\int_0^\infty\left[u_{11}(k) + k_s^{(3)^2}u_{31}(k)\right]J_1(kr)\,dk \qquad \text{(A-10a)}$$

$$u_\theta^{(h)} = \frac{F_r(\omega)}{4\pi\rho_3\omega^2} \sin\theta \frac{1}{r} \int_0^\infty \left[u_{11}(k) + k_s^{(3)2} u_{31}(k)\right] J_1(kr)\,dk$$

$$- \frac{F_r(\omega)}{4\pi\rho_3\omega^2} \sin\theta \int_0^\infty u_{31}(k)\, k J_0(kr)\,dk \qquad \text{(A-10b)}$$

and

$$u_z^{(h)} = -\frac{F_r(\omega)}{4\pi\rho_3\omega^2} \cos\theta \int_0^\infty u_{21}(k)\, k J_1(kr)\,dk\,, \qquad \text{(A-10c)}$$

where

$$k_s^{(3)} = \omega / c_s^{(3)}\,,$$

in which $c_s^{(3)}$ is the shear wave velocity in the lower half-space.

Similarly, the vector displacement for a vertical point source (n = 0) is given by

$$u_z^{(v)} = \frac{F_z(\omega)}{4\pi\rho_3\omega^2} \int_0^\infty u_{20}(k)\, k J_0(kr)\,dk \qquad \text{(A-11a)}$$

and

$$u_r^{(v)} = \frac{F_z(\omega)}{4\pi\rho_3\omega^2} \int_0^\infty u_{10}(k)\, k J_1(kr)\,dk\,. \qquad \text{(A-11b)}$$

APPENDIX B: EVALUATION OF WAVENUMBER INTEGRALS OF THE BESSEL FUNCTION TYPE BY THE MODIFIED CLENSHAW-CURTIS METHOD

I. THE WAVENUMBER INTEGRAL

Wavenumber integrals arise in the calculation of response of elastic media to a line or point excitation. In the latter case, the integrand is the product of the kernel F(k,z) and a Bessel function of the first kind, order *n*:

$$I = \int_0^\infty F(k,z) J_n(kr)\, dk, \tag{B-1}$$

where *z* and *r* are the vertical and horizontal distance between the source and the detector, respectively. This integral can be split into two parts:

$$I = \int_0^\kappa F(k,z) J_n(kr)\, dk + \int_\kappa^\infty F(k,z) J_n(kr)\, dk \tag{B-2}$$

where κ is a large wavenumber exceeding the real part of all poles of the kernel.

Conventional quadrature methods are either helpless or inefficient for this type of integral for the following reasons:

(1) Dense oscillations are present in both the Bessel function $J_n(kr)$ and the kernel F(k,z);

(2) There are sharp peaks in the kernel F(k,z);

(3) If the source and detector have the same depth, the leading term of the kernel F(k,z) does not decay for a large wavenumber *k*. It behaves as O(1) for displacement components due to a concentrated force, O(k) for stress components due to a concentrated force, or displacement components due to a volume source. Multiplying the leading term of the kernel by the factor $O(k^{-1/2})$ from the Bessel function, the integrand behaves either as $O(k^{-1/2})$ or $O(k^{1/2})$. In the latter case, the

integral will not converge if it is evaluated numerically with truncation at a finite value of wavenumber.

The Modified Clenshaw-Curtis (M. C.-C.) integration method is aimed at evaluating the above wavenumber integrals accurately and efficiently. This method has been recognized as the most efficient method of integration among schemes with similar objectives (Dravinski and Mossessian, 1988). In addition, none of the present quadrature schemes is able to handle the infinite tail when the integrand does not decay at large wavenumbers.

II. M. C.-C. METHOD: FINITE INTERVALS

Consider

$$I_1 = \int_0^{\kappa} F(k,z)J_n(kr)\,dk, \tag{B-3}$$

In the M. C.-C. method, the kernel F(k,z) is represented by a finite sum of the Chebyshev polynomials in κ. The resulting integral involving Chebyshev polynomials and Bessel functions is evaluated analytically, to avoid the numerical fitting of the Bessel functions. The accuracy of the quadrature is controlled by the decay rate of the expansion coefficients of the Chebyshev polynomials (in ascending order). The subdividing of the interval and the increasing (doubling) of the order of the polynomials are adaptive such that sample points are distributed rationally according to the irregularities of the kernel and that no previous function evaluations are wasted in the fitting process. More details of the formulation and algorithm for this part of the M. C.-C. method can be found in Xu and Mal (1985).

III. M. C.-C. METHOD: INFINITE TAIL

The problem of the infinite tail was solved in Xu and Mal (1987) for the case involving sinusoidal\cosinusoidal functions (line source, i.e., the two-dimensional problem). The

treatment of the infinite tail for the Bessel functions (point source, i.e., the three-dimensional problem) is presented below.

The remaining part of *I*,

$$I_2 = \int_{\kappa}^{\infty} F(k,z) J_n(kr)\,dk\,; \qquad \text{for } \kappa > 0, \quad r > 0\,, \tag{B-4}$$

is to be treated similarly to that for I_1. However, two additional steps are needed: converting the Bessel function into products of polynomials and sinusoidal/cosinusoidal functions, and the infinite interval to a finite one.

The Bessel functions of order 0 and 1 can be accurately represented (for kr > 4) as follows

$$J_n(kr) = \sqrt{\frac{2}{\pi kr}}\left[P_n(kr)\cos\left(kr - \frac{n\pi}{2} - \frac{\pi}{4}\right) - Q_n(kr)\sin\left(kr - \frac{n\pi}{2} - \frac{\pi}{4}\right)\right]. \tag{B-5}$$

In Equation (B-5) P_n and Q_n have the form

$$P_n\left(\frac{4}{t}\right) = a_0^{(n)} + a_2^{(n)}t^2 + a_4^{(n)}t^4 + a_6^{(n)}t^6 + a_8^{(n)}t^8 + a_{10}^{(n)}t^{10} \tag{B-6}$$

$$Q_n\left(\frac{4}{t}\right) = a_1^{(n)}t + a_3^{(n)}t^3 + a_5^{(n)}t^5 + a_7^{(n)}t^7 + a_9^{(n)}t^9 + a_{11}^{(n)}t^{11}, \tag{B-7}$$

where $a_m^{(n)}$, m = 0, 1, ..., 11, n = 0, 1 are known constants.

On the other hand, it can be shown from wave propagation theory that for large *k*, the asymptotic expression for F(k) is given by

$$F(k,z) = e^{-kz}\left[A + B/k + C/k^2 + D/k^3 + E/k^4 + O\left(k^{-5}\right)\right], \tag{B-8}$$

where A, B, C, D, and E are constants.

Combining Eqs. (B-5)–(B-8), the integrand becomes:

$$F(k,z)J_n(kr) \doteq k^{\nu} e^{-kw} \sum_{m=0}^{N} A_m k^{-m}, \tag{B-9}$$

where $w = z - ir$, $i = \sqrt{(-1)}$, ν is -0.5 or 0.5, depending on the combination of component and source types. N is the assigned highest order of the Chebyshev polynomials. In practice, $N = 4$ or 8 is chosen. A_m's are constant coefficients.

Next, let's make a change of variable: $q = 1/k$. Then the interval $[\kappa,\infty]$ in the k domain maps to $[0, 1/\kappa]$ in the q domain. A polynomial type function of q can be extracted from the integrand as

$$G(q) \doteq F(kz)J_n(kr)e^{kw}k^{-\nu} = \sum_{m=0}^{N} A_m q^m.$$

This function can be fitted more easily by Chebyshev polynomials:

$$G(q) = \sum_{m=0}^{N} C_m T_m(\tau), \tag{B-11}$$

where $T_m(\tau)$ are Chebyshev polynomials, C_m are the Chebyshev coefficients, and the interval $[0, 1/\kappa]$ in the q domain has been converted to $[-1, 1]$ in the r domain by linear transformation (see Xu and Mal, 1985). The needed coefficients A_m's can be derived from C_m's by standard procedure.

Finally, from Eqs. (B-4) and (B-9)–(B-11), the evaluation of integral I_2 is reduced to the following:

$$I_2 = \sum_{m=0}^{N} A_m S_m, \tag{B-12}$$

where $$S_m = \int_{\kappa}^{\infty} k^{\nu-m} e^{-kw} dk = \frac{1}{w^{\nu+1}} \Gamma(\nu+1-m, \kappa w). \tag{B-13}$$

In Equation (B-13), $\Gamma(\nu + 1 - m, \kappa w)$ is known as the incomplete Gamma function. Its first argument, $\alpha = \nu + 1 - m$, is real and the second, $\mu = \kappa w$, complex. Properties of the incomplete Gamma function can be found in Abramowitz and Stegun (1972) and Gradshteyn and Ryzhik (1980). Its numerical evaluation is divided into two cases. For small $|\mu|$,

$$\Gamma(\alpha, \mu) \doteq \Gamma(\alpha) - \sum_{n=0}^{\infty} \frac{(-1)^n \mu^{\alpha+n}}{n!(\alpha+n)}, \tag{B-14}$$

where $\Gamma(\alpha)$ is the well known complete Gamma function. For large $|\mu|$,

$$\Gamma(\alpha,\mu) \doteq e^{-\mu}\mu^{\alpha}\left[\frac{1}{\mu+}\,\frac{1-\alpha}{1+}\,\frac{1}{\mu+}\,\frac{2-\alpha}{1+}\,\frac{2}{\mu}\,\cdots\right] \tag{B-15}$$

This concludes the implementation of the M. C.-C. method for the Bessel function type wavenumber integrals.

LIST OF ILLUSTRATIONS AND TABLES

Figure 7 Geometry of a dipping low-velocity layer at an angle of 40 degrees with respect to the horizontal r-axis in an unbounded medium.

Figure 8 Comparisons of horizontal and vertical component synthetic seismograms. a) Radial- and b) vertical-component seismograms for a horizontal point force in the presence of a dipping low-velocity layer in an unbounded medium. c) Radial- and d) vertical component seismograms for a horizontal point force in an unbounded medium.

Figure 9 Instantaneous signal propagation vectors as two-axis hodogram plots for a horizontal force in the presence of a low-velocity layer in an unbounded medium. Hodograms were produced from waveforms calculated for receiver depths 7.5 m apart; a) from −35 m through 2.5 m, and b) from 10 m through 47.5 m.

Figure 10 Instantaneous signal propagation vectors as two-axis hodogram plots for a horizontal force in the presence of a dipping low-velocity layer in an unbounded medium. Hodograms produced from 300 Hz waveforms calculated for receiver depths 7.5 m apart, from −35 m through −12.5 m.

Figure 11 Radial- and vertical-component seismograms produced by a 300 Hz horizontal force pulse signal in the presence of a dipping low-velocity layer in an unbounded medium.

TABLE I. Formation parameters.

Region	v_p (m/s)	v_s (m/s)	ρ (kg/m^3)	Q
Layer	2653	1490	2420	10
Upper and Lower Medium	3794	2074	2630	40

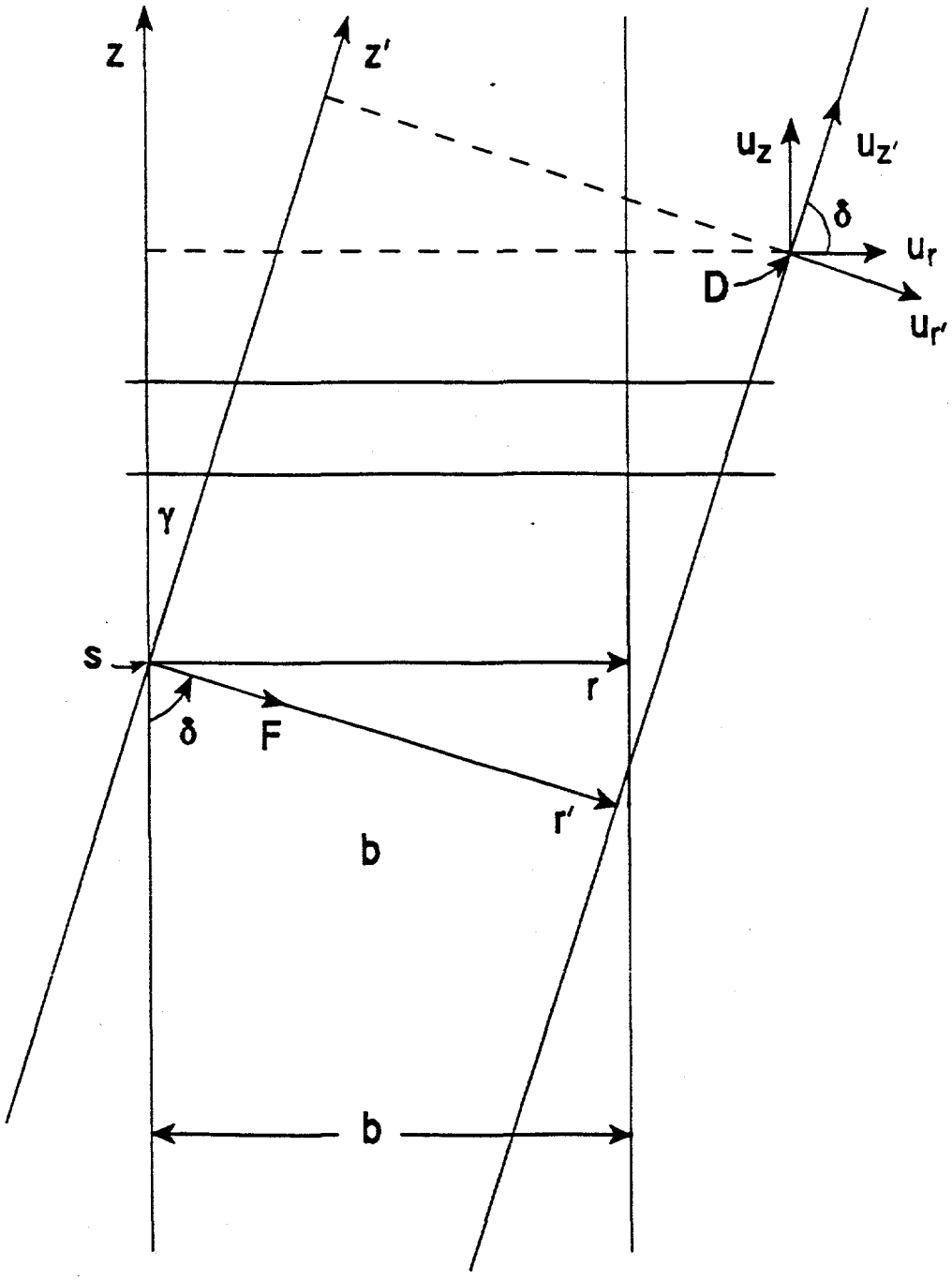

Figure 1

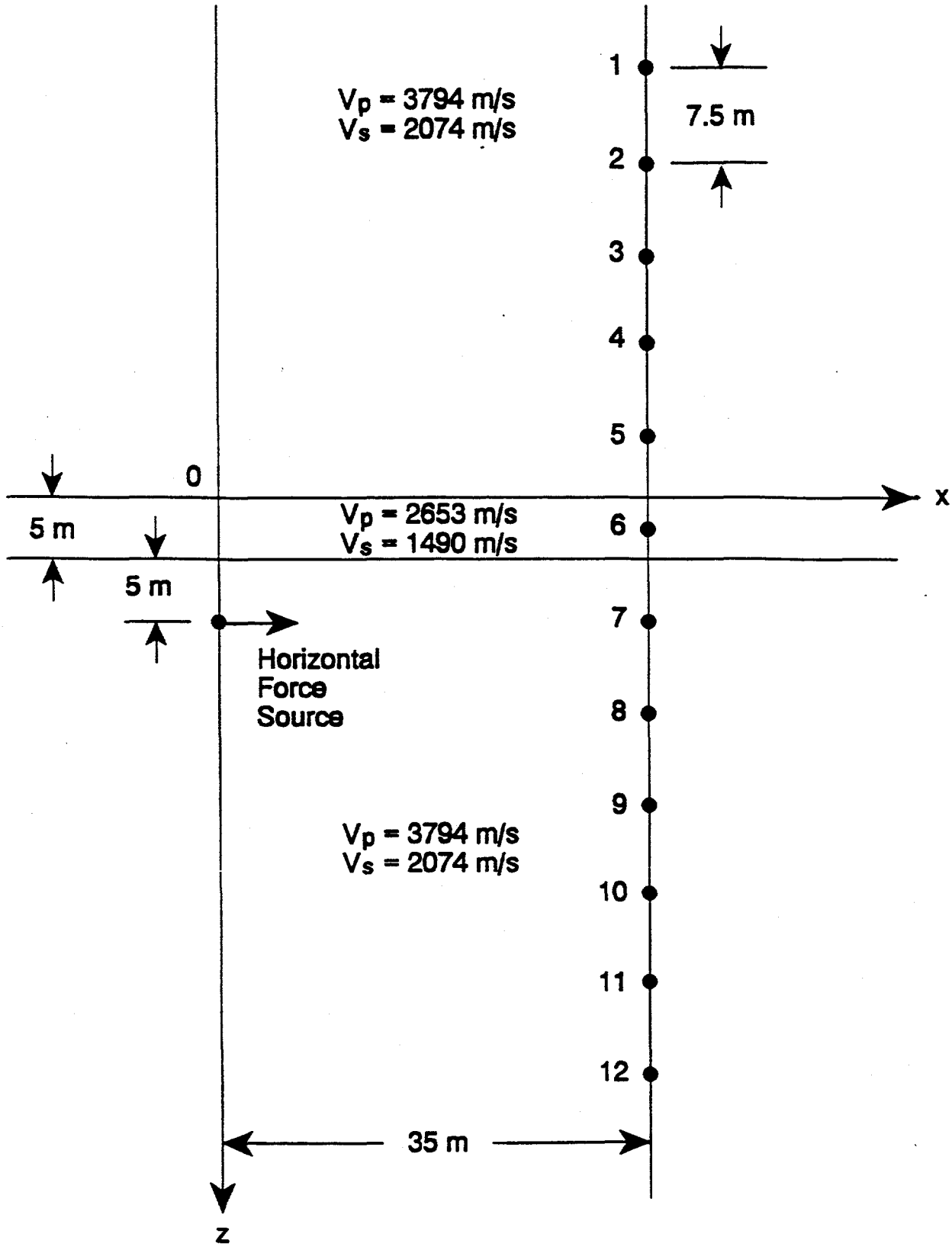
Vp = 3794 m/s
Vs = 2074 m/s
1
7.5 m
2
3
4
5
0
x
5 m
Vp = 2653 m/s
Vs = 1490 m/s
6
5 m
7
Horizontal
Force
Source
8
9
Vp = 3794 m/s
Vs = 2074 m/s
10
11
12
35 m
z

Figure 2

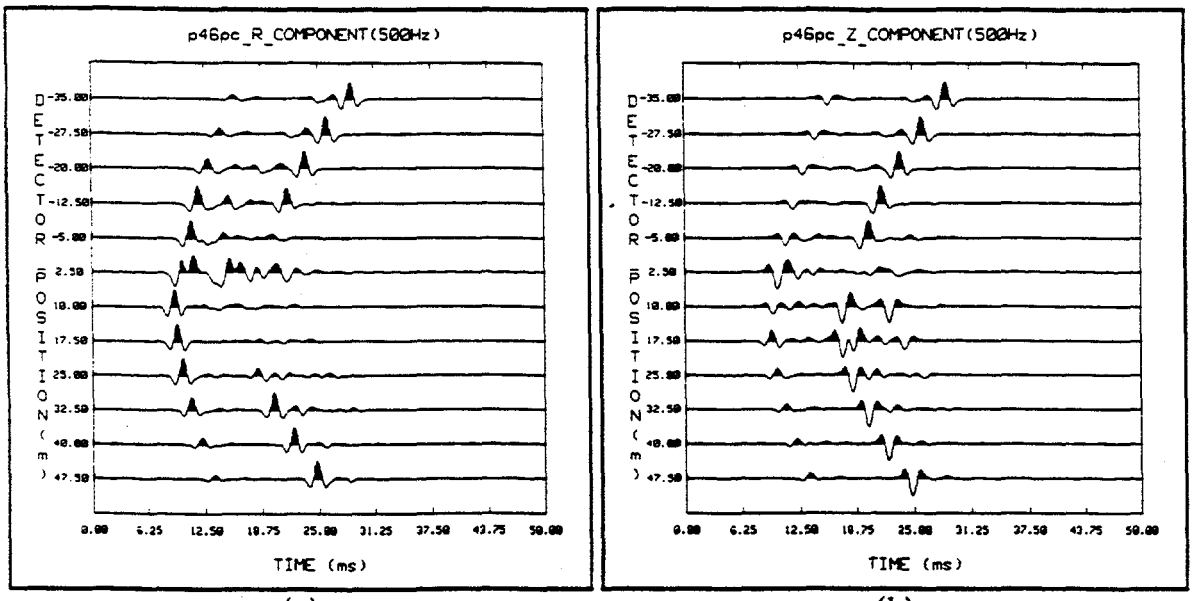

(a)

(b)

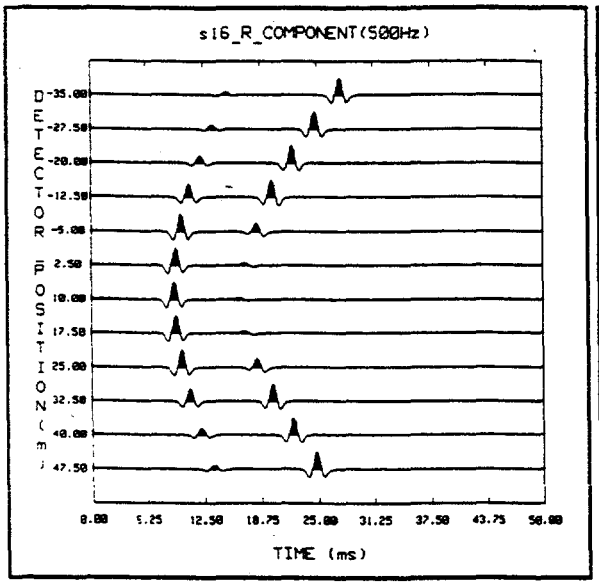

(c)

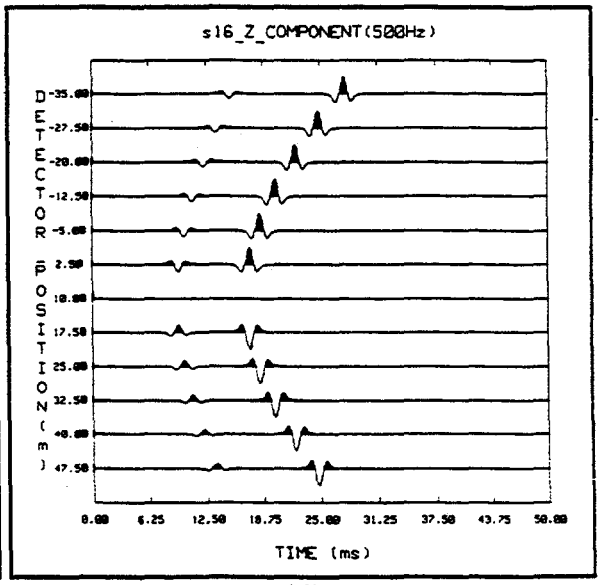

(d)

Figure 3

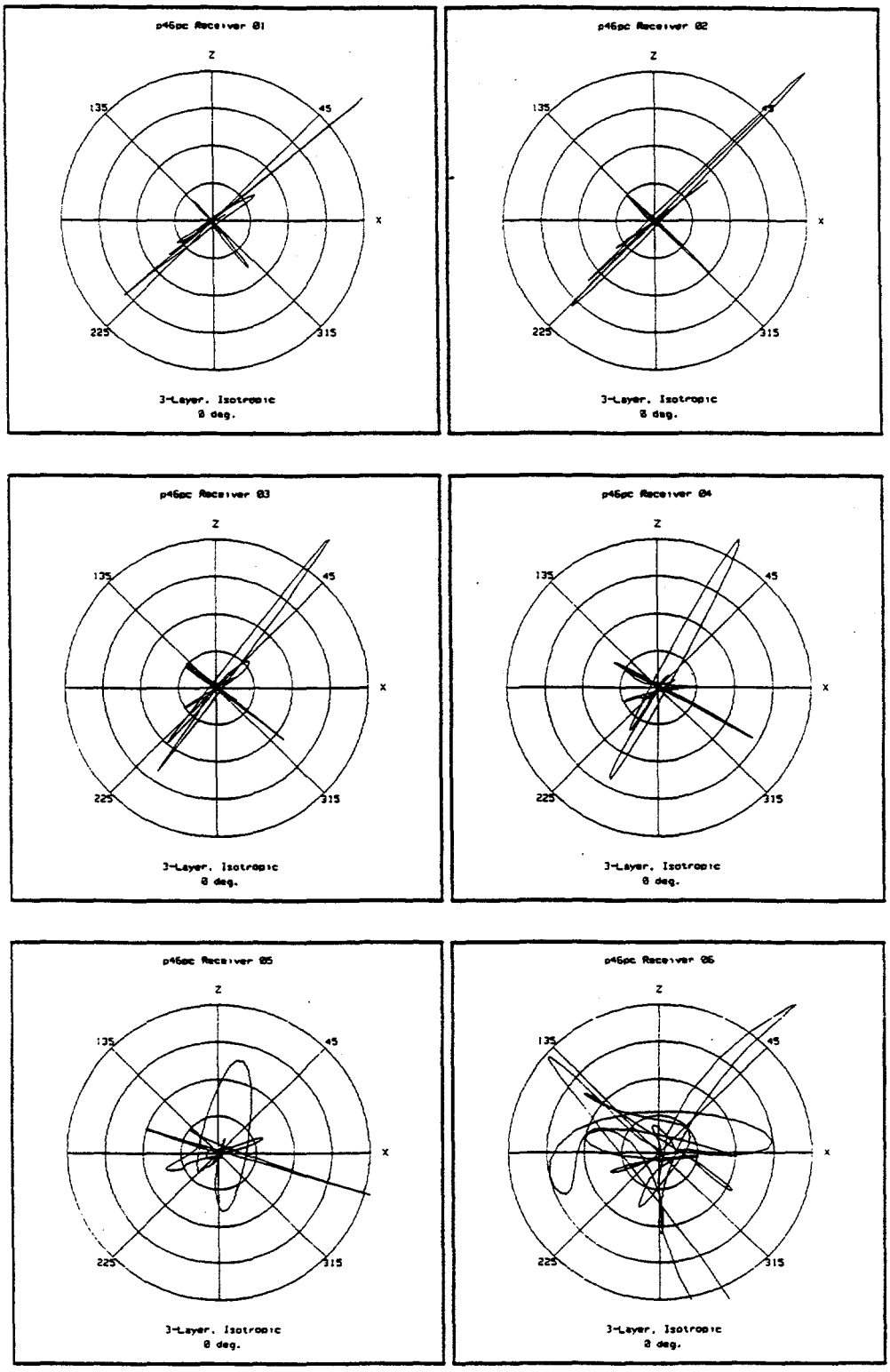
p46pc Receiver 01
Z
135
45
225
315
X
3-Layer, Isotropic
0 deg.
p46pc Receiver 02
Z
135
225
315
X
3-Layer, Isotropic
0 deg.
p46pc Receiver 03
Z
135
45
225
315
X
3-Layer, Isotropic
0 deg.
p46pc Receiver 04
Z
135
45
225
315
X
3-Layer, Isotropic
0 deg.
p46pc Receiver 05
Z
135
45
225
315
X
3-Layer, Isotropic
0 deg.
p46pc Receiver 06
Z
135
45
225
315
X
3-Layer, Isotropic
0 deg.

Figure 4a

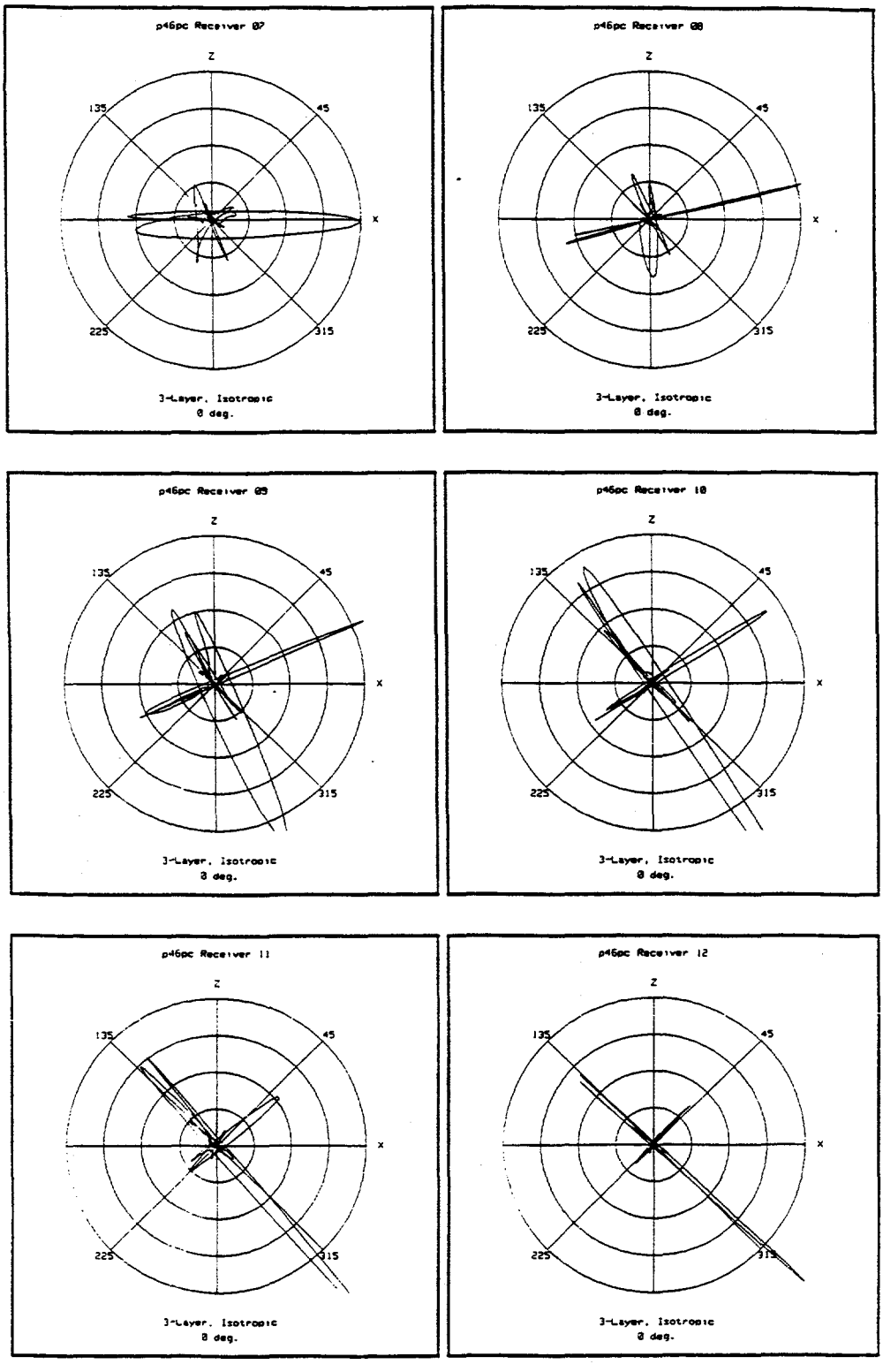
p46pc Receiver 07
Z
135
45
X
225
315
3-Layer, Isotropic
0 deg.
p46pc Receiver 08
Z
135
45
X
225
315
3-Layer, Isotropic
0 deg.
p46pc Receiver 09
Z
135
45
X
225
315
3-Layer, Isotropic
0 deg.
p46pc Receiver 10
Z
135
45
X
225
315
3-Layer, Isotropic
0 deg.
p46pc Receiver 11
Z
135
45
X
225
315
3-Layer, Isotropic
0 deg.
p46pc Receiver 12
Z
135
45
X
225
315
3-Layer, Isotropic
0 deg.

Figure 4b

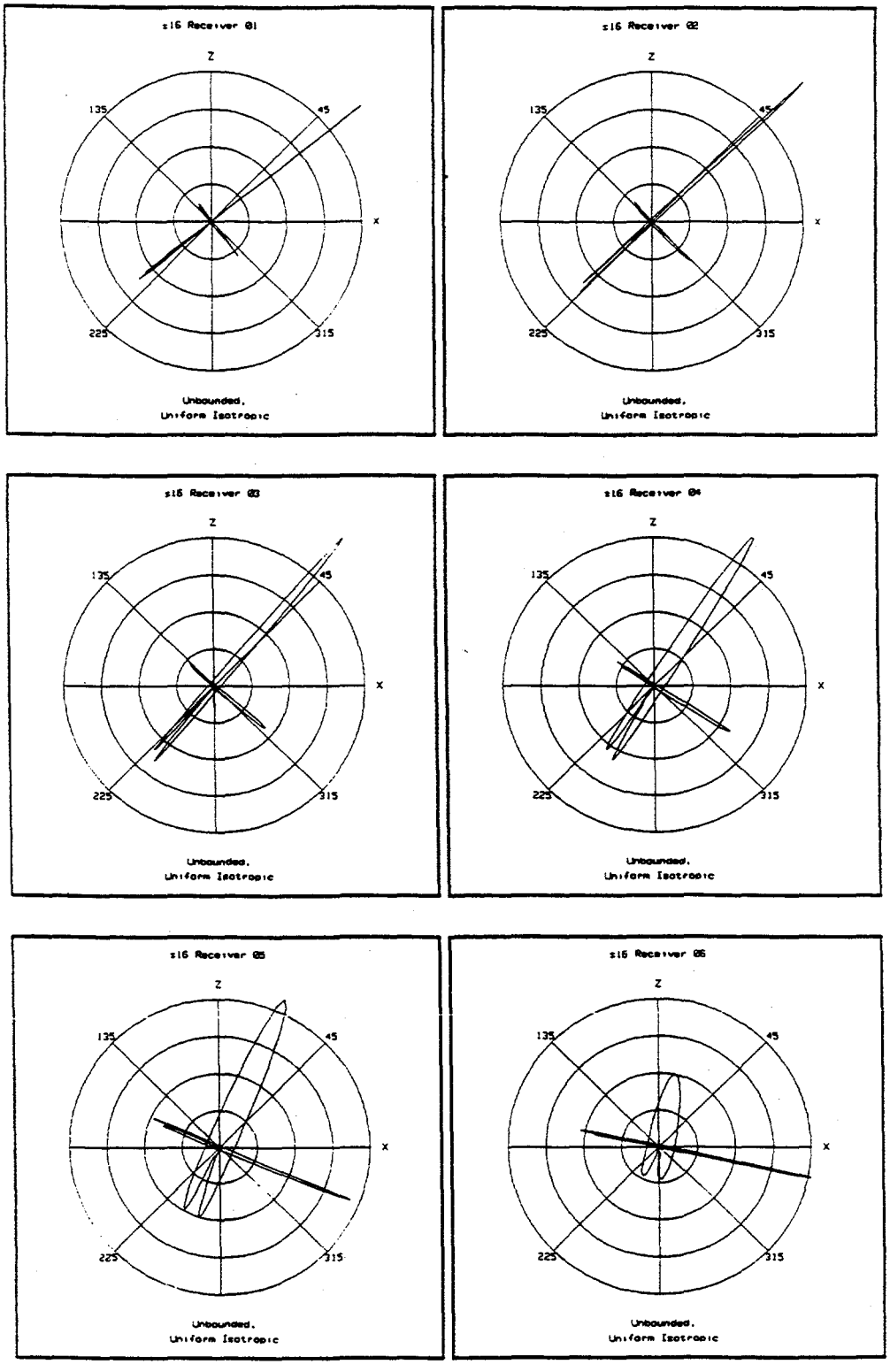
s16 Receiver 01
Z
135
45
X
225
315
Unbounded,
Uniform Isotropic
s16 Receiver 02
Z
135
45
X
225
315
Unbounded,
Uniform Isotropic
s16 Receiver 03
Z
135
45
X
225
315
Unbounded,
Uniform Isotropic
s16 Receiver 04
Z
135
45
X
225
315
Unbounded,
Uniform Isotropic
s16 Receiver 05
Z
135
45
X
225
315
Unbounded,
Uniform Isotropic
s16 Receiver 06
Z
135
45
X
225
315
Unbounded,
Uniform Isotropic

Figure 5a

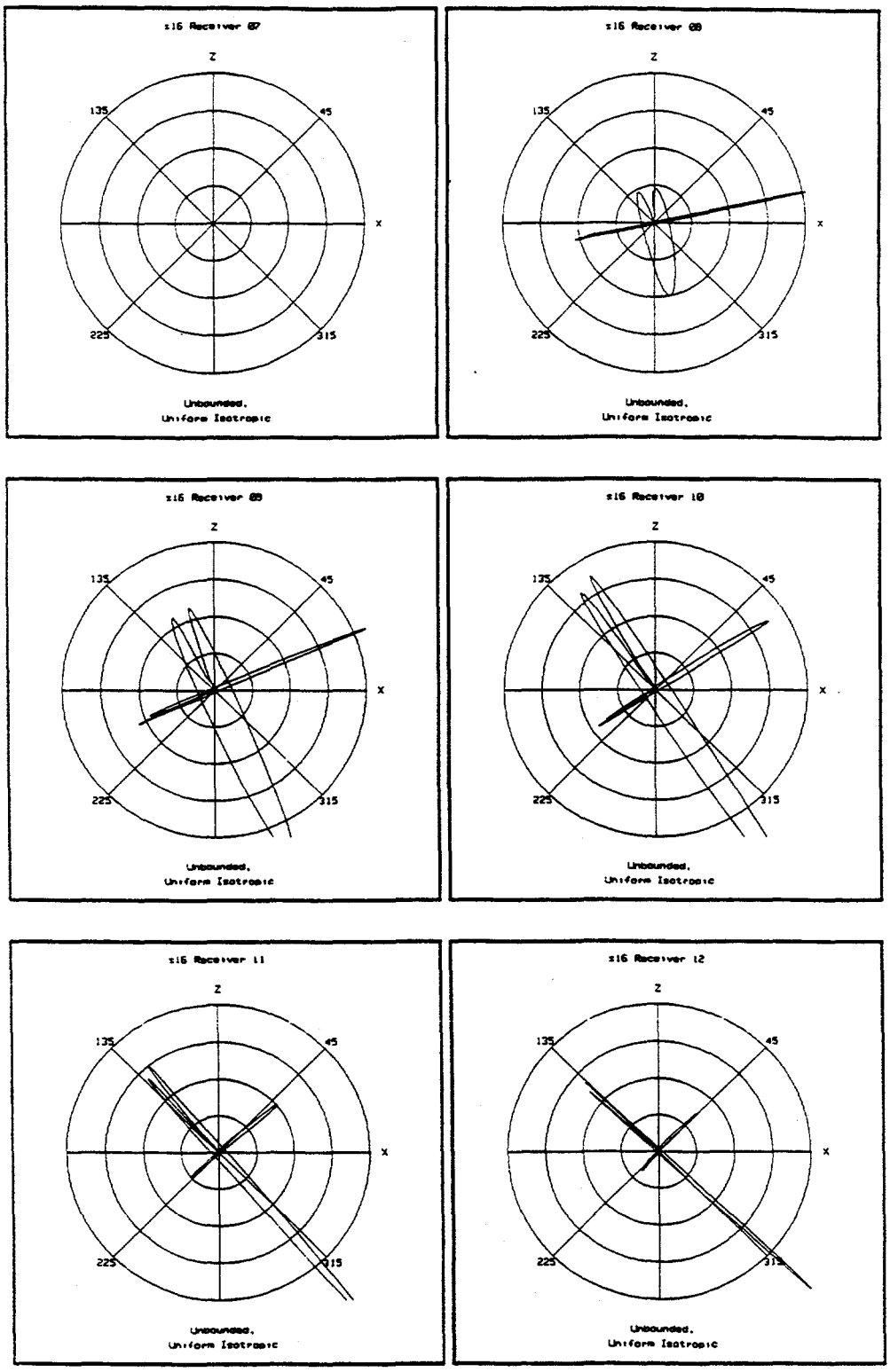

Figure 5b

(a)

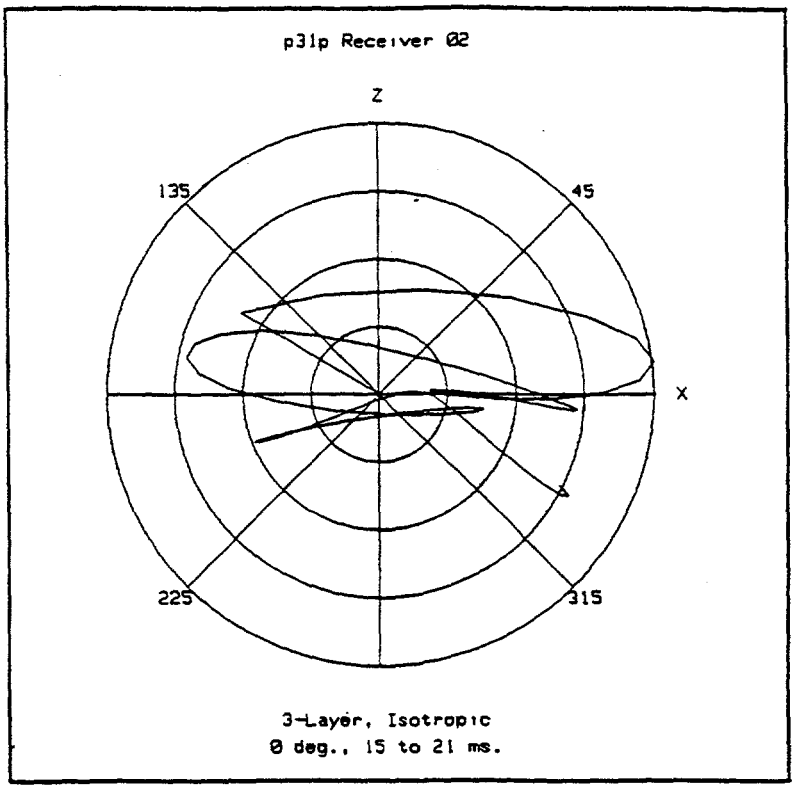
p31p Receiver 02
Z
135
45
X
225
315
3-Layer, Isotropic
0 deg., 15 to 21 ms.

(b)

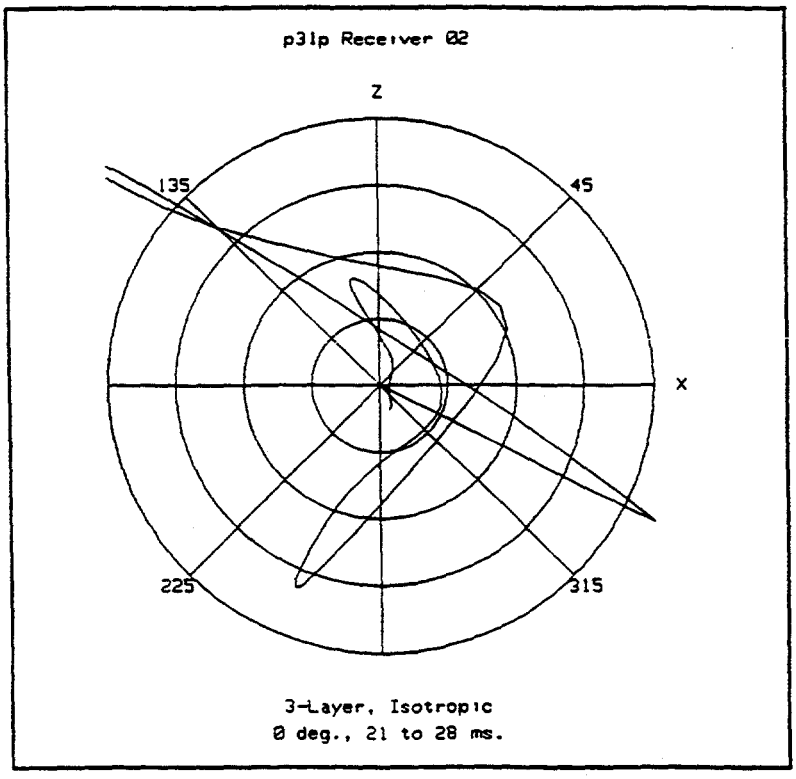
p31p Receiver 02
Z
135
45
X
225
315
3-Layer, Isotropic
0 deg., 21 to 28 ms.

Figure 6

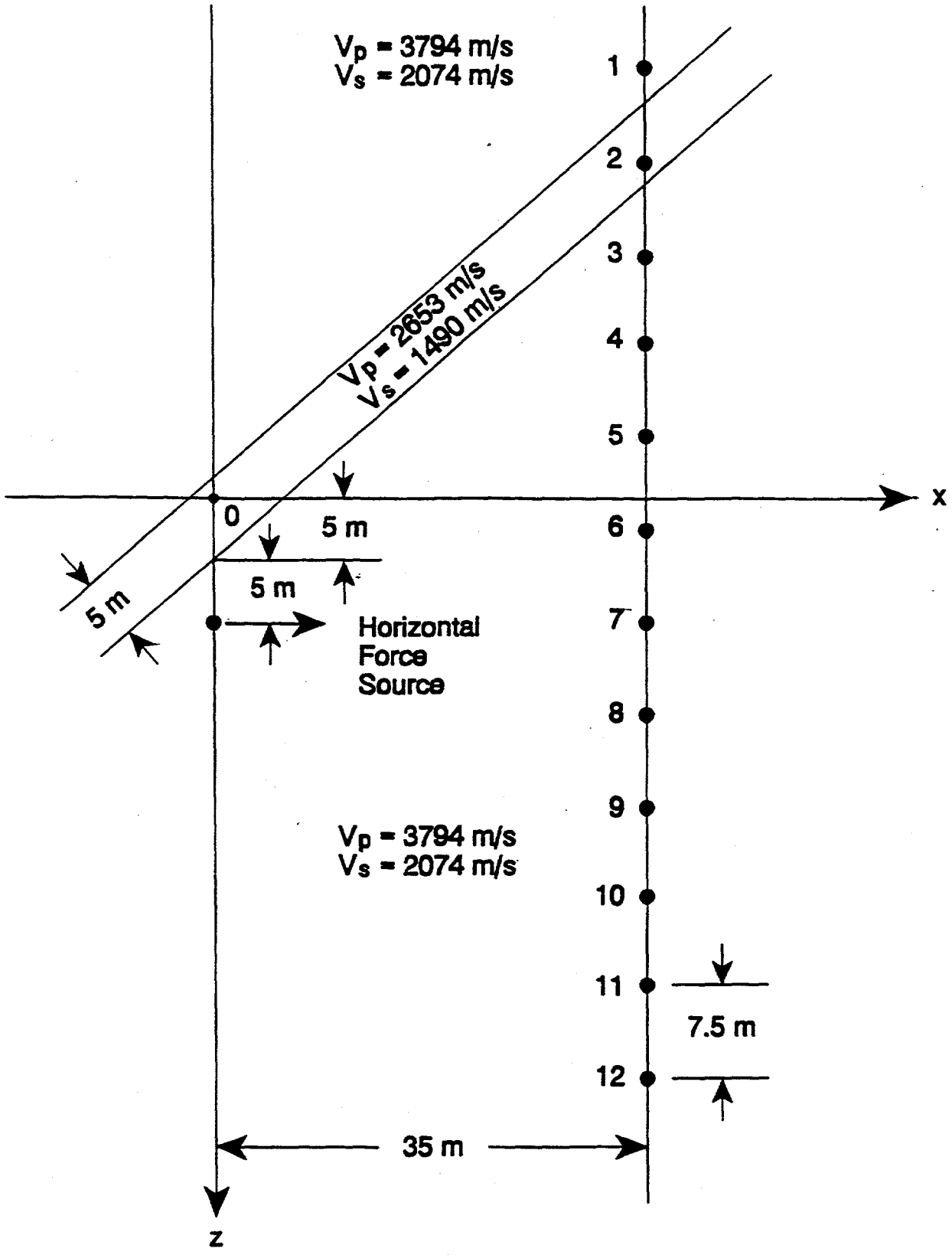
Vp = 3794 m/s
Vs = 2074 m/s
Vp = 2653 m/s
Vs = 1490 m/s
1
2
3
4
5
6
7
8
9
10
11
12
x
0
5 m
5 m
5 m
Horizontal
Force
Source
Vp = 3794 m/s
Vs = 2074 m/s
7.5 m
35 m
z

Figure 7

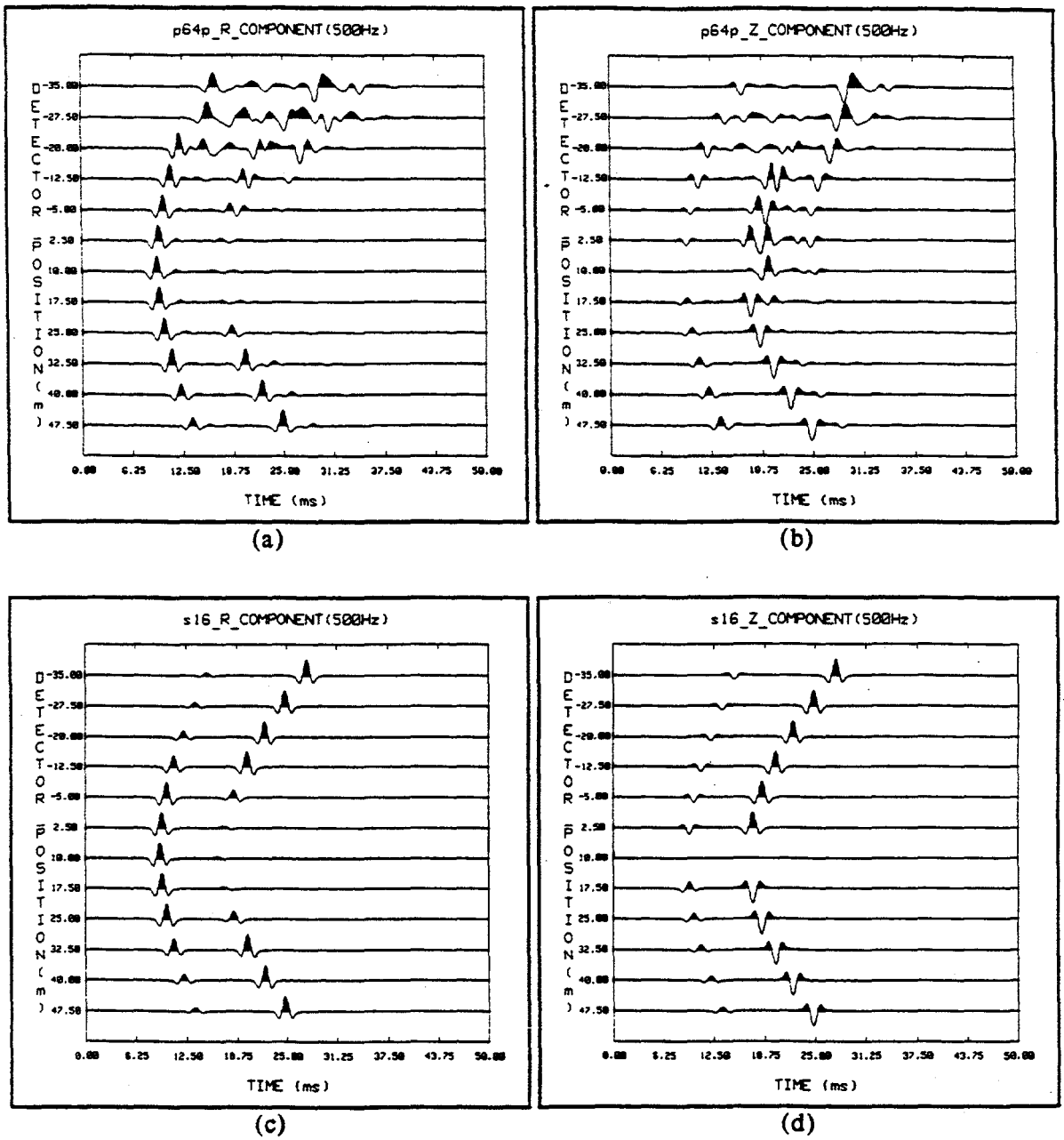
p64p_R_COMPONENT(500Hz)
p64p_Z_COMPONENT(500Hz)
s16_R_COMPONENT(500Hz)
s16_Z_COMPONENT(500Hz)
DETECTOR POSITION (m)
TIME (ms)
(a)
(b)
(c)
(d)

Figure 8

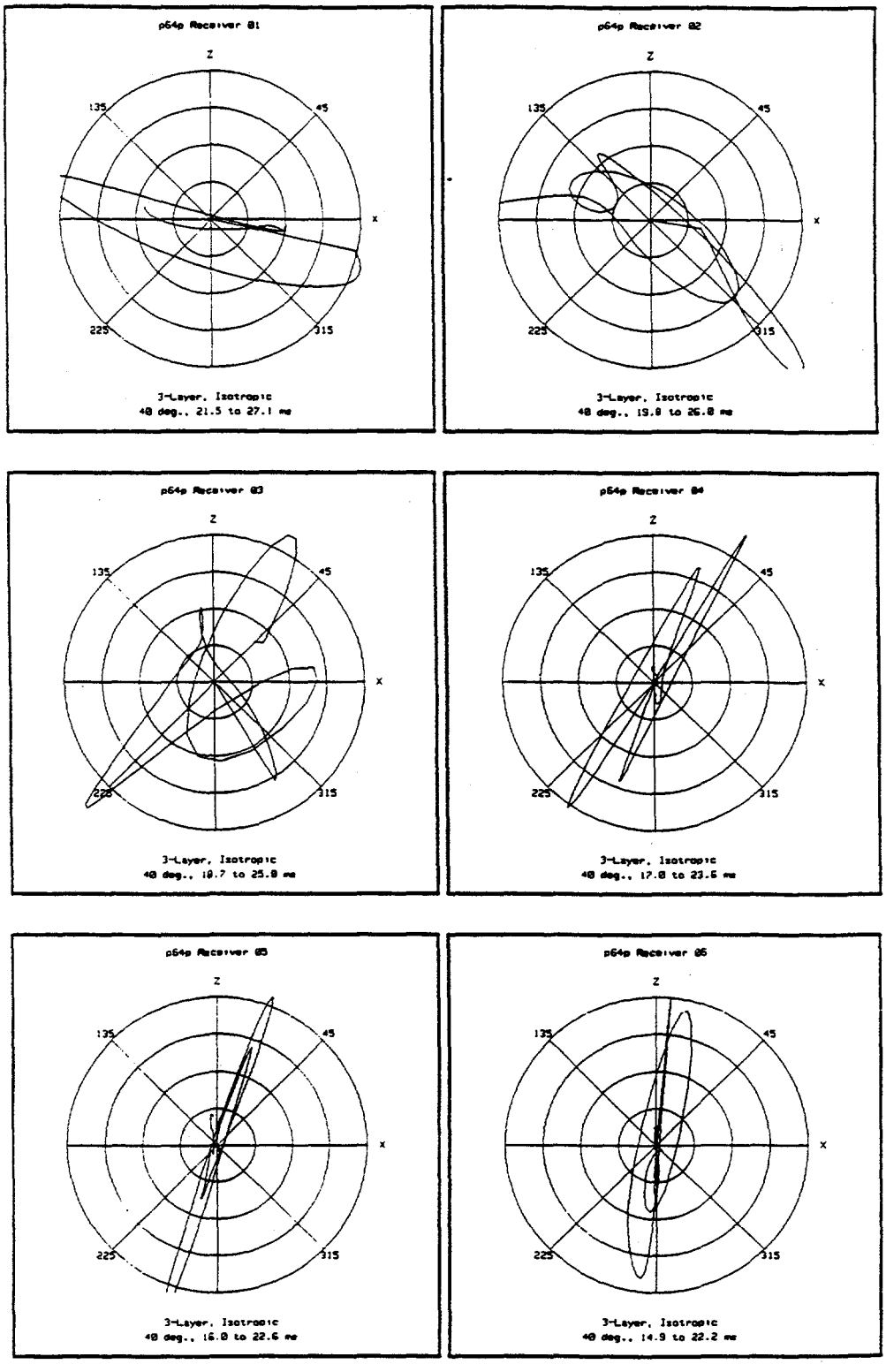
p64p Receiver 01
Z
135
45
x
225
315
3-Layer, Isotropic
40 deg., 21.5 to 27.1 ms
p64p Receiver 02
Z
135
45
x
225
315
3-Layer, Isotropic
40 deg., 19.8 to 26.8 ms
p64p Receiver 03
Z
135
45
x
225
315
3-Layer, Isotropic
40 deg., 18.7 to 25.8 ms
p64p Receiver 04
Z
135
45
x
225
315
3-Layer, Isotropic
40 deg., 17.8 to 23.6 ms
p64p Receiver 05
Z
135
45
x
225
315
3-Layer, Isotropic
40 deg., 16.8 to 22.6 ms
p64p Receiver 06
Z
135
45
x
225
315
3-Layer, Isotropic
40 deg., 14.9 to 22.2 ms

Figure 9a

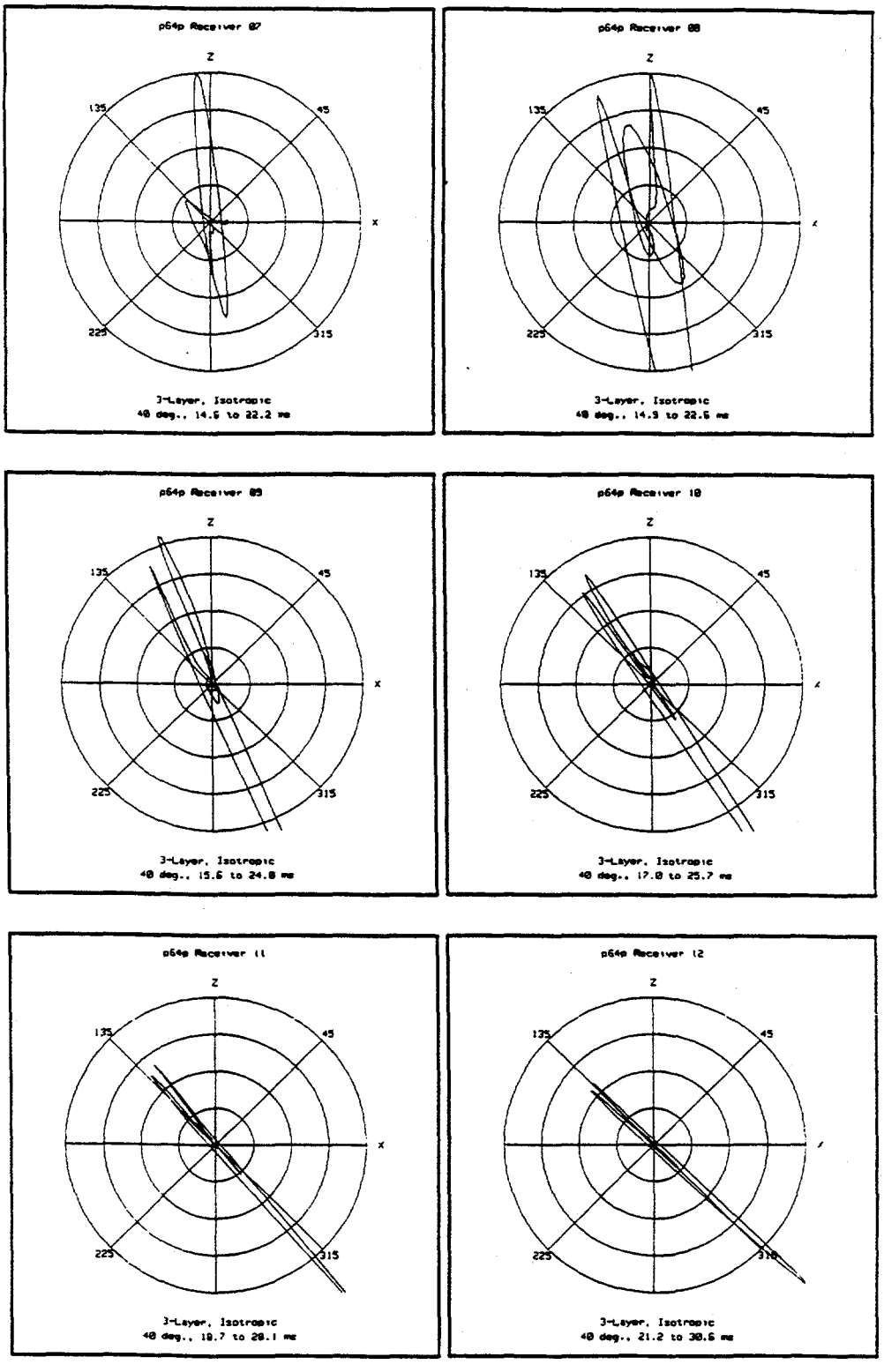
p64p Receiver 07
Z
135
45
X
225
315
3-Layer, Isotropic
40 deg., 14.6 to 22.2 ms
p64p Receiver 08
Z
135
45
X
225
315
3-Layer, Isotropic
40 deg., 14.9 to 22.6 ms
p64p Receiver 09
Z
135
45
X
225
315
3-Layer, Isotropic
40 deg., 15.6 to 24.8 ms
p64p Receiver 10
Z
135
45
X
225
315
3-Layer, Isotropic
40 deg., 17.0 to 25.7 ms
p64p Receiver 11
Z
135
45
X
225
315
3-Layer, Isotropic
40 deg., 18.7 to 28.1 ms
p64p Receiver 12
Z
135
45
X
225
315
3-Layer, Isotropic
40 deg., 21.2 to 30.6 ms

Figure 9b

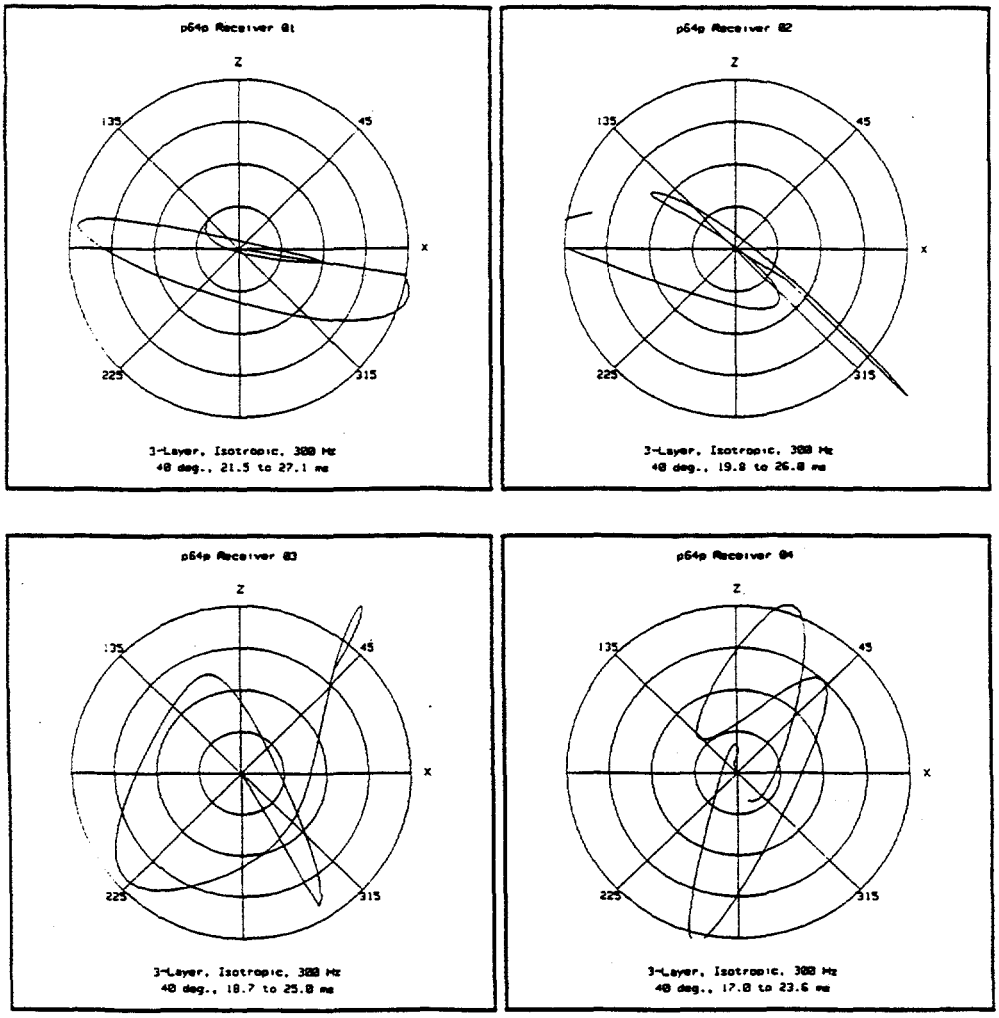
p64p Receiver 01
Z
135
45
x
225
315
3-Layer, Isotropic, 300 Hz
40 deg., 21.5 to 27.1 ms
p64p Receiver 02
Z
135
45
x
225
315
3-Layer, Isotropic, 300 Hz
40 deg., 19.8 to 26.8 ms
p64p Receiver 03
Z
135
45
x
225
315
3-Layer, Isotropic, 300 Hz
40 deg., 18.7 to 25.8 ms
p64p Receiver 04
Z
135
45
x
225
315
3-Layer, Isotropic, 300 Hz
40 deg., 17.8 to 23.6 ms

Figure 10

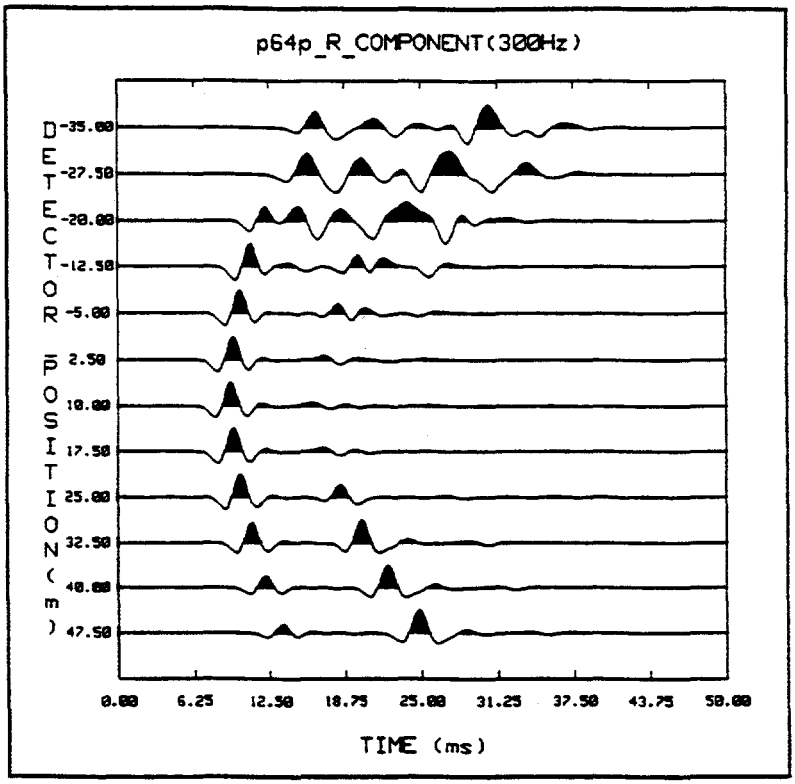
p64p_R_COMPONENT(300Hz)
DETECTOR POSITION(m)
-35.00
-27.50
-20.00
-12.50
-5.00
2.50
10.00
17.50
25.00
32.50
40.00
47.50
0.00
6.25
12.50
18.75
25.00
31.25
37.50
43.75
50.00
TIME (ms)

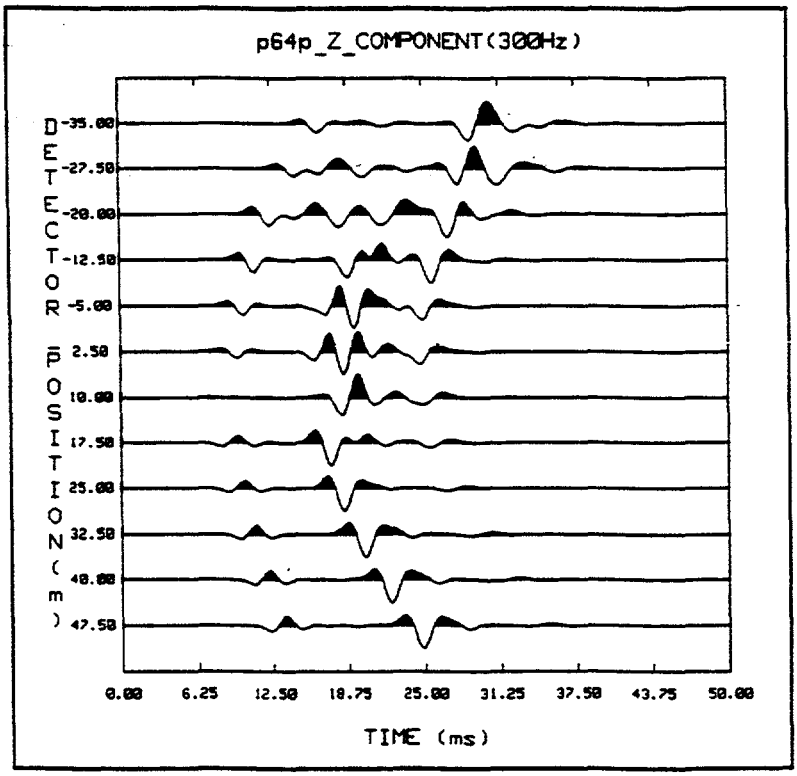
p64p_Z_COMPONENT(300Hz)
DETECTOR POSITION(m)
-35.00
-27.50
-20.00
-12.50
-5.00
2.50
10.00
17.50
25.00
32.50
40.00
47.50
0.00
6.25
12.50
18.75
25.00
31.25
37.50
43.75
50.00
TIME (ms)

Figure 11